

# Diffraction by a rigid strip in a plate modelled by Mindlin theory

Ian Thompson\*,

Department of Mathematical Sciences, University of Liverpool,  
Liverpool L69 7ZL, UK

November 6, 2020

## Abstract

We consider a plane flexural wave incident on a semi-infinite rigid strip in a Mindlin plate. The boundary conditions on the strip lead to three Wiener–Hopf equations, one of which decouples, leaving a scalar problem and a  $2 \times 2$  matrix problem. The latter is solved using a simple method based on quadrature. The far field diffraction coefficient is calculated and some numerical results are presented. We also show how the results reduce to the simpler Kirchhoff model in the low frequency limit.

## 1 Introduction

The theory of wave propagation through elastic media plays an important role in the nondestructive evaluation techniques widely used in engineering [1, chapter 7],[2]. These methods detect cracks and other defects by measuring and analysing the response to a signal transmitted into a structure. To correctly interpret these scattering patterns, it is first necessary to understand how the wave field behaves when it interacts with inhomogeneities. Such interactions are difficult to capture using direct numerical simulations, due to the intricate structure of the field close to an inhomogeneity, and the singularities that can occur at sharp tips or corners. To overcome this, the geometrical theory of diffraction [3, 4] assembles the field inside a complicated structure using solutions to *canonical problems*, obtained by analytical means. Each canonical problem describes how waves interact with a small number of inhomogeneities, such as edges, corners or cracks (often just one), and the solution yields a *diffraction coefficient* which shows how the field varies as a function of position, angle of incidence and any other parameters that appear in the problem (such as flexural rigidity, Poisson’s ratio, etc.).

Canonical diffraction problems in acoustics and electromagnetism have a long history, dating back to Sommerfeld’s work on diffraction by a half-plane, published in 1896 [5]. Solutions to numerous other canonical diffraction problems became available following the introduction of the Wiener–Hopf technique in 1931 [6, 7]. Interest in elastodynamic wave diffraction is a relatively recent development. The first paper on the subject considered diffraction by a semi-infinite crack and appeared in 1977 [8]. For reviews of subsequent papers in this field, see [9, 10]. The first paper to consider diffraction in thin elastic media, which is important for modelling propagation through structures such as aeroplane wings and panels in submarine hulls, was published in 1994 [11] and considered diffraction by rigid strips and cracks in plates modelled by Kirchhoff theory. The results for cracks were later generalised to certain classes of anisotropic media in [12, 13].

In this article, we consider diffraction caused by a plane wave striking a semi-infinite rigid strip in a plate modelled by Mindlin theory [14, 15].<sup>1</sup> Mindlin theory is valid at higher frequencies than the classical Kirchhoff theory. From a mathematical perspective, the main difference between the two models is that Mindlin represents the flexural wave field using a combination of three types of mode, whereas Kirchhoff uses two. Three boundary conditions must be applied along the faces of the

---

\*[ian.thompson@liv.ac.uk](mailto:ian.thompson@liv.ac.uk)

<sup>1</sup>Curiously, the title of item [7] in the bibliography of [9] suggests that the former contains a treatment of the same problem. Following communication with the authors listed (I D Abrahams and A N Norris), it has been established that the article was started but not completed; the status of the bibliography entry in [9] (‘submitted’) is incorrect.

strip, leading to a system of three Wiener–Hopf equations. One of these decouples, leaving a scalar problem and a  $2 \times 2$  matrix problem. The scalar problem can be solved using a standard procedure [6], but matrix Wiener–Hopf problems are notoriously difficult, and as yet no general method for solving these has been discovered. The main obstacle is the factorisation of a matrix function  $L(\alpha)$ , called the kernel, into a product  $L^+(\alpha)L^-(\alpha)$ , where the elements of  $L^+(\alpha)$  are analytic on and above a certain contour in the complex plane (usually the real line with indentations), and the elements of  $L^-(\alpha)$  are analytic on and below the same contour. Certain restricted classes can be factorised; these include meromorphic matrices and those that can be expressed in Khrapkov form [16, 17, 9]. The matrix kernel that appears in the diffraction problem considered here has three pairs of branch points, and its entries are somewhat complicated. It is very unlikely that it can be reduced to Khrapkov form. To overcome this problem, we introduce a simple but accurate approximate scheme that solves the matrix Wiener–Hopf equation directly, bypassing the need for a kernel factorisation. The diffraction coefficient for the tip of the rigid strip is obtained and a uniform asymptotic representation for the far field is constructed. Numerical results are presented, using a nondimensionalisation scheme which eliminates most of the physical parameters describing the plate.

## 2 Waves in Mindlin plates

Consider the motion of a plate with thickness  $h$ , density  $\rho$  and Poisson’s ratio  $\nu$ , modelled using Mindlin theory [14], [18, section 8.3]. The undisturbed midplane occupies  $z = 0$ , and the deformation can be expressed in the form [19]

$$\mathbf{U} = z\Psi(x, y, t) + W(x, y, t)\mathbf{e}_z, \quad (1)$$

where  $W$  is the transverse displacement and the in-plane vector of rotations is given by

$$\Psi = \Psi_x(x, y, t)\mathbf{e}_x + \Psi_y(x, y, t)\mathbf{e}_y. \quad (2)$$

We will assume time-harmonic motion; thus for any function  $F(x, y, t)$ , we write

$$F(x, y, t) = \text{Re}[f(x, y)e^{-i\omega t}], \quad (3)$$

where  $\omega$  is the angular frequency. The convention of using corresponding upper and lower case letters in this way is not entirely standard in plate theory (often  $\psi$  and  $w$  are used to represent time-dependent quantities), but it does introduce a degree of consistency. Following [20], we introduce the quantities

$$c_s = \kappa \left( \frac{\mu}{\rho} \right)^{1/2}, \quad c_p = \left[ \frac{E}{\rho(1 - \nu^2)} \right]^{1/2}, \quad k_s = \frac{\omega}{c_s}, \quad k_p = \frac{\omega}{c_p} \quad \text{and} \quad k_f = \left( \frac{\rho h \omega^2}{D} \right)^{1/4}. \quad (4)$$

Here,  $\kappa$  is a shear correction factor [18, pp. 484, 492–3]. The Lamé constant  $\mu$  and bending stiffness  $D$  are defined in terms of the Young modulus  $E$  via

$$\mu = \frac{E}{2(1 + \nu)} \quad \text{and} \quad D = \frac{Eh^3}{12(1 - \nu^2)}. \quad (5)$$

Note that  $k_f$  is the wavenumber from Kirchhoff theory, and is  $O(\sqrt{\omega})$  whereas  $k_s$  and  $k_p$  are  $O(\omega)$ . Waves in a Mindlin plate can now be described using the three Helmholtz equations [14, 20]

$$(\nabla^2 + k_j^2)w_j = 0, \quad j = 1, 2 \quad \text{and} \quad (\nabla^2 + k_3^2)\phi = 0. \quad (6)$$

The transverse displacement is then given by

$$w = w_1 + w_2, \quad (7)$$

and components of the in-plane rotation vector are reconstructed via

$$\psi_x = \frac{\partial}{\partial x}(A_1 w_1 + A_2 w_2) + \frac{\partial \phi}{\partial y} \quad \text{and} \quad \psi_y = \frac{\partial}{\partial y}(A_1 w_1 + A_2 w_2) - \frac{\partial \phi}{\partial x}, \quad (8)$$

where

$$A_j = -1 + k_s^2/k_j^2. \quad (9)$$

The wavenumbers appearing in the Helmholtz equations are given by

$$k_1^2 = \frac{k_p^2 + k_s^2}{2} + \sqrt{k_f^4 + \frac{(k_p^2 - k_s^2)^2}{4}}, \quad k_2^2 = \frac{k_p^2 + k_s^2}{2} - \sqrt{k_f^4 + \frac{(k_p^2 - k_s^2)^2}{4}}, \quad (10)$$

and

$$k_3^2 = \kappa^2 k_1^2 k_2^2 / k_p^2. \quad (11)$$

Clearly,  $k_1^2$  is always positive, whereas  $k_2^2 < 0$  at low frequencies. At the cut-on, where  $k_2 = 0$ , we have  $k_f^4 = k_s^2 k_p^2$  and  $k_1^2 = k_p^2 + k_s^2$ . The first of these reduces to

$$\omega = \sqrt{12} c_s / h, \quad (12)$$

and the second then yields

$$k_1 h = \sqrt{12 + 6\kappa^2(1 - \nu)}. \quad (13)$$

However, it is noted in [15, section 5.07] that Mindlin theory is only expected to give accurate results if the wavelength is at least twice the plate thickness, which corresponds to  $k_1 \leq \pi/h$ . Since  $\frac{1}{2} > \nu > -1$  [21, section 2.4], it follows that  $k_2$  is imaginary for all frequencies that satisfy this bound. We take  $k_2$ , and therefore also  $k_3$ , to be positive imaginary. Finally, we observe that  $k_1 > k_s$ , because (10) shows that  $k_1^2 - k_s^2 > 0$ . In view of the fact that

$$\frac{\kappa^2 k_s^2}{k_p^2} = \frac{E}{\mu(1 - \nu^2)} = \frac{2}{1 - \nu}, \quad (14)$$

this shows that  $|k_3| > |k_2|$ . We also have

$$A_1 < 0, \quad A_2 < 0 \quad \text{and} \quad A_1 - A_2 > 0. \quad (15)$$

### 3 The diffraction problem

Consider a Mindlin plate that extends throughout the  $(x, y)$  plane, for  $|z| \leq h/2$ , with a rigid barrier occupying the strip  $y = 0$ ,  $x > 0$ ,  $|z| \leq h/2$ ; see figure 1. The plane wave

$$w^i(x, y) = e^{ik_1(x \cos \Theta + y \sin \Theta)}, \quad 0 \leq \Theta \leq \pi, \quad (16)$$

propagates through the plate and is incident at angle  $\Theta$  on the rigid barrier. This is a propagating mode because  $k_1$  is real. There are no contributions to the incident field with wavenumber  $k_2$  or  $k_3$  because these are evanescent modes. We seek a scattered field such that all components of the total displacement vanish on the rigid strip, that is

$$w^t(x, 0) = \psi_x^t(x, 0) = \psi_y^t(x, 0) = 0, \quad \text{for } x > 0. \quad (17)$$

Here, the superscript ‘t’ indicates that the field includes contributions from both incident and scattered waves, i.e.

$$w^t = w^i + w, \quad \psi_x^t = \psi_x^i + \psi_x \quad \text{and} \quad \psi_y^t = \psi_y^i + \psi_y. \quad (18)$$

The incident components of  $\psi_x$  and  $\psi_y$  can be obtained using (8) and (16); thus

$$\psi_x^i = iA_1 k_1 \cos \Theta e^{ik_1(x \cos \Theta + y \sin \Theta)} \quad \text{and} \quad \psi_y^i = iA_1 k_1 \sin \Theta e^{ik_1(x \cos \Theta + y \sin \Theta)}. \quad (19)$$

The scattered field must satisfy the Sommerfeld radiation condition, meaning there can be no contributions that are incoming toward  $y = 0$  or that grow as  $|y| \rightarrow \infty$ .

To ensure a unique solution, we also require a *tip condition*, which restricts the behaviour of the field in the vicinity of the origin. An appropriate condition is that the strain energy density must be

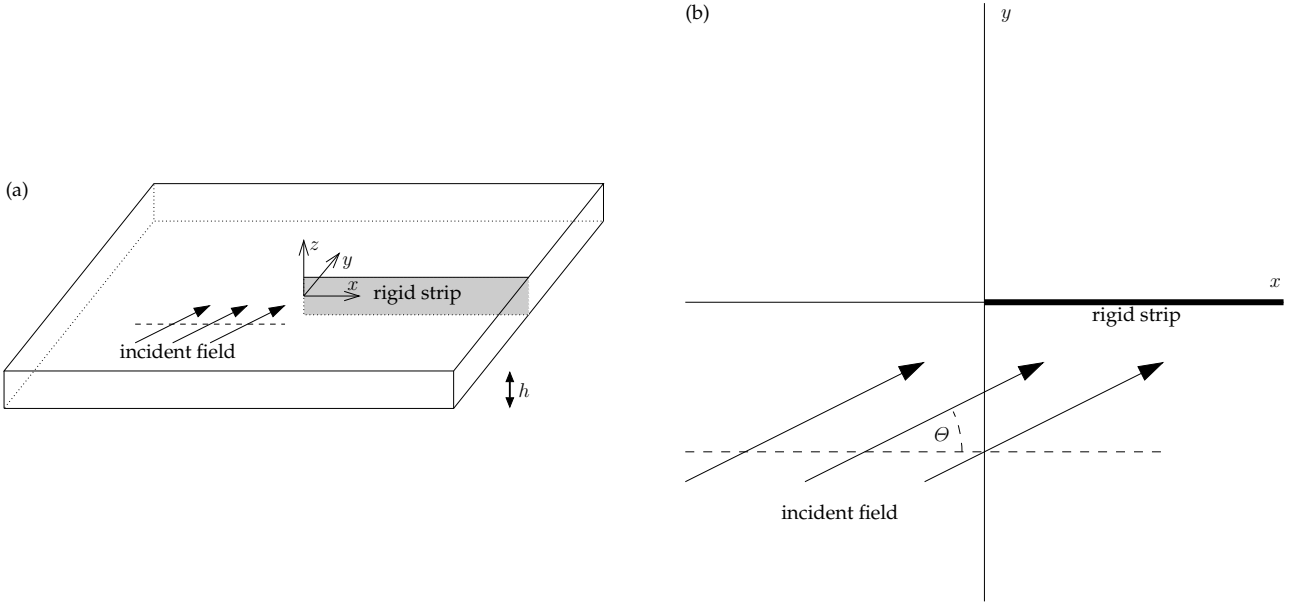


Figure 1: (a) Schematic diagram of the diffraction problem, showing the rigid strip and flexural plane wave inside a plate of thickness  $h$ . (b) Cross-section of the plate, for fixed  $z$ .

integrable [11]. Now the plate strain energy function is given in [14, eqn. (18)], and using equation (12) from the same paper, we can write it in the form

$$\mathcal{S} = \frac{D}{2} \left[ \left( \frac{\partial \Psi_x}{\partial x} \right)^2 + \left( \frac{\partial \Psi_y}{\partial y} \right)^2 + 2\nu \frac{\partial \Psi_x}{\partial x} \frac{\partial \Psi_y}{\partial y} + \frac{1-\nu}{2} \left( \frac{\partial \Psi_x}{\partial y} + \frac{\partial \Psi_y}{\partial x} \right)^2 \right] + \frac{\kappa^2 \mu h}{2} \left[ \left( \frac{\partial W}{\partial x} + \Psi_x \right)^2 + \left( \frac{\partial W}{\partial y} + \Psi_y \right)^2 \right]. \quad (20)$$

Since  $\Psi_x$ ,  $\Psi_y$  and  $W$  are displacements, each must remain finite throughout the plate. In particular, as  $r = \sqrt{x^2 + y^2} \rightarrow 0$ , it must be the case that  $W = O(r^\eta)$ , with  $\eta \geq 0$  and similarly for  $\Psi_x$  and  $\Psi_y$ . It then follows that  $r^2 \mathcal{S} \rightarrow 0$  as  $r \rightarrow 0$ . Consequently, a solution in which all displacements remain bounded automatically has an integrable strain energy density. We can make some further deductions by differentiating (8) to obtain

$$\frac{\partial \psi_x}{\partial y} - \frac{\partial \psi_y}{\partial x} = \nabla^2 \phi = -k_3^2 \phi \quad (21)$$

and

$$\frac{\partial \psi_x}{\partial x} + \frac{\partial \psi_y}{\partial y} = \nabla^2 (A_1 w_1 + A_2 w_2) = -k_s^2 w + k_1^2 w_1 + k_2^2 w_2. \quad (22)$$

Since  $\psi_x$ ,  $\psi_y$  and  $w$  are known to be bounded (and  $w = w_1 + w_2$ ), it follows immediately that  $\phi(x, 0)$ ,  $w_1(x, 0)$  and  $w_2(x, 0)$  can at most have integrable singularities at the origin (here ‘integrable’ refers to integrability in one dimension, not over a two-dimensional region as in the discussion of strain energy density, above). Consequently,  $w_j$  and  $\phi$  can be represented as Fourier integrals, which converge for all  $x$  except possibly  $x = 0$ . However, it may be that derivatives of  $w_j$  and  $\phi$  do not have Fourier representations that are valid on  $y = 0$ . This leads to a technicality relating to the order in which limits are taken, which will be addressed in the next section.

For the remainder of the paper, it is convenient to work with dimensionless coordinates

$$x_* = k_1 x \quad \text{and} \quad y_* = k_1 y. \quad (23)$$

The Helmholtz equations (6) become

$$\left( \frac{\partial^2}{\partial x_*^2} + \frac{\partial^2}{\partial y_*^2} + q_j^2 \right) w_j = 0, \quad j = 1, 2, \quad \text{and} \quad \left( \frac{\partial^2}{\partial x_*^2} + \frac{\partial^2}{\partial y_*^2} + q_3^2 \right) \phi = 0, \quad (24)$$

where the dimensionless wavenumbers are given by

$$q_j = k_j/k_1, \quad j = 1, 2, 3. \quad (25)$$

Here we have introduced new symbols because it will be convenient to refer to both dimensional and nondimensional wavenumbers in places. The scaling (23) does not affect the boundary conditions for the total field, because these are homogeneous. However, we must express the incident field in nondimensional form; that is

$$w^i(x, y) = e^{i(x_* \cos \Theta + y_* \sin \Theta)}. \quad (26)$$

Henceforth, all coordinates are taken to be dimensionless, and we will omit the subscript ‘\*’.

Finally, we introduce the nondimensional frequency

$$\omega^* = h\omega/c_s, \quad (27)$$

where  $c_s$  is given by (4). Now (14) can be used to express  $k_p^2/k_s^2$  in terms of the Poisson ratio  $\nu$ , and similarly

$$k_f^4/k_s^4 = 6\kappa^2(1 - \nu)/(\omega^*)^2, \quad (28)$$

having used (5). The ratios  $k_s^2/k_j^2$  and  $k_j/k_1$  appearing in (9) and (25) can both be expressed in terms of  $\omega^*$ ,  $\nu$  and  $\kappa$ . The dimensional physical parameters  $E$ ,  $h$  and  $\rho$  are all eliminated. To determine the maximum value for  $\omega^*$ , we rearrange (10) to form a quartic equation for  $k_j$  and then set this to  $\pi/h$  (recalling that  $k_1 = \pi/h$  corresponds to a wavelength equal to twice the plate thickness; see section 2). In this way, we obtain

$$(1 - \nu)\kappa^2(\omega^*)^4 - [2\pi^2 + (1 - \nu)\kappa^2(\pi^2 + 12)](\omega^*)^2 + 2\pi^4 = 0. \quad (29)$$

The frequency at which  $k_2 = 0$  corresponds to  $\omega^* = \sqrt{12}$ , (see (12)), and here the left-hand side of (29) is negative. Since it is positive at  $\omega^* = 0$ , it follows that there are two positive roots, one to the left and one to the right of  $\sqrt{12}$ . The larger root corresponds to  $k_2 = \pi/h$  and is unimportant.

## 4 Integral solutions to the Helmholtz equation

The components of the scattered field will now be represented as inverse Fourier transforms. These representations can be derived by applying Fourier transforms in  $x$  to (6), solving the resulting ordinary differential equations, taking inverse transforms and using the radiation condition to eliminate unphysical terms. Technically, one must introduce damping in order to do this, for example by assuming that  $\cos \Theta > 0$  and writing  $q_1 = 1 + i\varepsilon$ , with  $\varepsilon > 0$ . Without damping, forward Fourier transforms will not converge due to the presence of plane waves in the problem. The same procedure is often used in solving the Sommerfeld half-plane problem (see e.g. [6, Section 2.2]), so we do not repeat it here. Instead, we simply observe that the transform functions may be different in the upper and lower halves of the  $(x, y)$  plane, so the appropriate form for  $w_j$  is

$$w_j(x, y) = \begin{cases} \frac{1}{2\pi} \int_{\Gamma} \hat{w}_j^u(\alpha) e^{-\gamma_j(\alpha)|y| - i\alpha x} d\alpha & \text{if } y > 0, \\ \frac{1}{2\pi} \int_{\Gamma} \hat{w}_j^l(\alpha) e^{-\gamma_j(\alpha)|y| - i\alpha x} d\alpha & \text{if } y < 0, \end{cases} \quad (30)$$

where

$$\gamma_j(\alpha) = (\alpha^2 - q_j^2)^{1/2}. \quad (31)$$

The contour  $\Gamma$  is the real line traversed from left to right, with indentations around singularities, including the branch points at  $\alpha = \pm 1$  (but not  $\alpha = \pm q_2$  or  $\alpha = \pm q_3$ , since these are imaginary). To satisfy the radiation condition,  $\gamma_j(\alpha)$  must be nonnegative real or negative imaginary for real arguments, in view of (3). Consequently, we take  $\gamma_j(0) = -iq_j$ , and the contour  $\Gamma$  is indented to pass over the branch point at  $\alpha = -1$  and under the branch point at  $\alpha = 1$ ; see figure 2a. Other indentations can be applied later, as necessary.

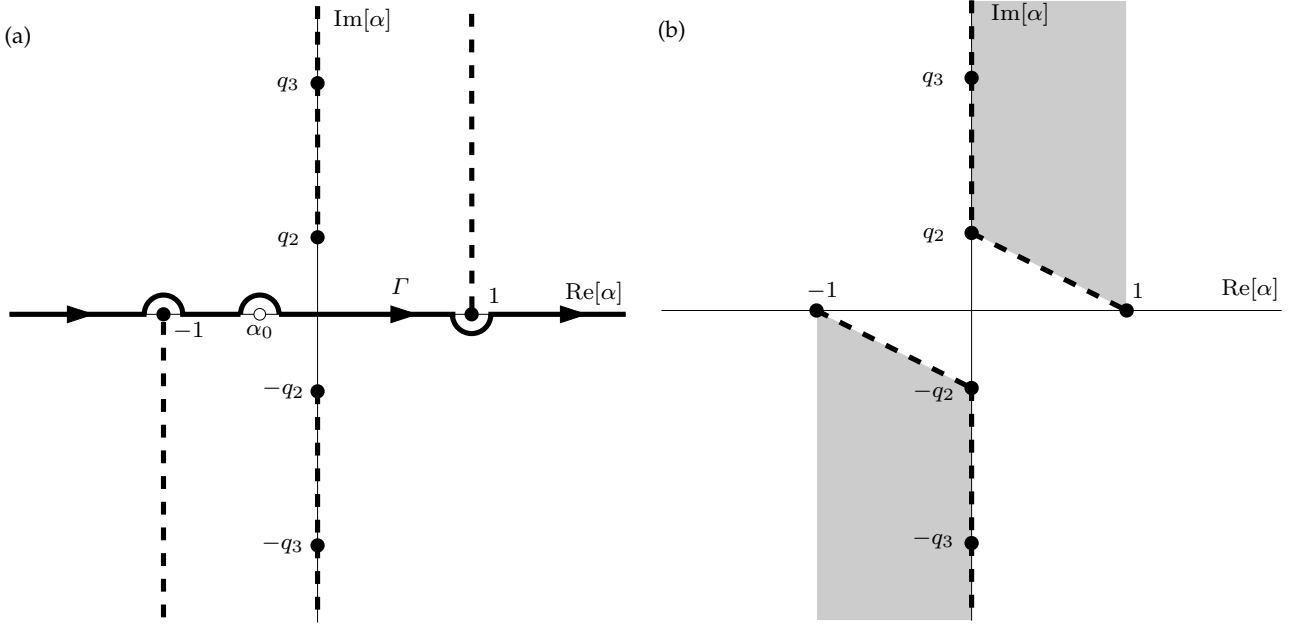


Figure 2: (a) The contour  $\Gamma$  in the  $\alpha$  plane, with vertical branch cuts. The directions of the indentations around the branch points are determined by the radiation condition. The appearance of a pole at  $\alpha = \alpha_0$  and the direction of the indentation around this singularity are discussed in section 5. (b) The adjusted branch cuts used in solving the matrix Wiener–Hopf equation. The shaded regions show where  $L(\alpha)$  differs from its value in the original configuration (a).

Now (30) satisfies the appropriate Helmholtz equation in (24), except possibly across  $y = 0$ . Since the plate itself is continuous for  $x < 0$ , the Helmholtz equation must hold on the half-line  $y = 0$ ,  $x < 0$ . To enforce continuity and differentiability here, we can employ Jordan’s lemma [22, Theorem 5.6], which shows that if  $y = 0$  then the contour  $\Gamma$  can be deformed in different directions for  $x > 0$  and  $x < 0$ . Let  $\mathcal{D}^+$  ( $\mathcal{D}^-$ ) represent the region consisting of all points on or above (on or below)  $\Gamma$ , and introduce the convention that a superscript ‘+’ or ‘−’ applied to a function denotes analyticity within  $\mathcal{D}^+$  or  $\mathcal{D}^-$ , respectively. In addition, any function  $f^\pm$  has the property that

$$f^\pm(\alpha)/\alpha^n \rightarrow 0 \quad \text{as} \quad \alpha \rightarrow \infty \in \mathcal{D}^\pm, \quad \text{for some} \quad n \in \{0, 1, 2, \dots\}. \quad (32)$$

This relatively weak condition allows us to address the fact that the limit  $y \rightarrow 0$  does not commute with all the integral representations employed below. To see how this works, suppose that

$$u(x, y) = \frac{1}{2\pi} \int_{\Gamma} \hat{u}(\alpha) e^{-\gamma_j(\alpha)|y| - i\alpha x} d\alpha \quad (33)$$

and

$$u(x, 0) = 0 \quad \text{for all} \quad x < 0. \quad (34)$$

In the limit  $y \rightarrow 0$ , it must be possible to evaluate the integral in (33) in such a way that no singularity contributions are collected for  $x < 0$ ; otherwise (34) could not be satisfied for *all* negative  $x$ . If the limit commutes with the integral, applying Jordan’s lemma shows that (34) is satisfied if  $\hat{u}(\alpha) = \hat{u}^+(\alpha)$  and  $\hat{u}(\alpha) \rightarrow 0$  as  $\alpha \rightarrow \infty \in \mathcal{D}^+$ . To relax the condition on the behaviour of  $\hat{u}^+(\alpha)$  at infinity, we indent the contour to pass above the origin and integrate in  $x$  to obtain

$$\int u(x, y) dx = C(y) + \frac{i}{2\pi} \oint_{\Gamma} \frac{\hat{u}^+(\alpha)}{\alpha} e^{-\gamma_j(\alpha)|y| - i\alpha x} d\alpha, \quad (35)$$

for an arbitrary function  $C$ . Then, if  $\hat{u}^+(\alpha)/\alpha \rightarrow 0$  as  $\alpha \rightarrow \infty \in \mathcal{D}^+$ , Jordan’s lemma yields

$$\int u(x, 0) dx = C(0), \quad (36)$$

and differentiating shows that  $u(x, 0) = 0$ . The process of integrating and differentiating in  $x$  can be applied repeatedly, and the end result is that  $u(x, 0) = 0$  for  $x < 0$  provided  $\hat{u}^+(\alpha)$  satisfies (32).

Let us now establish continuity of the displacement components  $w_j$  and their normal derivatives across the half-line  $y = 0$ ,  $x < 0$ . We have

$$w_j(x, y) - w_j(x, -y) = \frac{1}{2\pi} \int_{\Gamma} [\hat{w}_j^u(\alpha) - \hat{w}_j^\ell(\alpha)] e^{-\gamma_j(\alpha)|y|} e^{-i\alpha x} d\alpha, \quad (37)$$

and in the limit  $y \rightarrow 0$  this must evaluate to zero for all negative  $x$ . Therefore we write

$$\hat{w}_j^u(\alpha) - \hat{w}_j^\ell(\alpha) = 2T_j^+(\alpha), \quad (38)$$

where the factor 2 is included for algebraic convenience. Similarly, for  $y > 0$ , we have

$$\frac{\partial w_j}{\partial y}(x, y) - \frac{\partial w_j}{\partial y}(x, -y) = -\frac{1}{2\pi} \int_{\Gamma} \gamma_j(\alpha) [\hat{w}_j^u(\alpha) + \hat{w}_j^\ell(\alpha)] e^{-\gamma_j(\alpha)|y|} e^{-i\alpha x} d\alpha, \quad (39)$$

and continuity on  $y = 0$ ,  $x < 0$  is enforced by writing

$$\gamma_j(\alpha) [\hat{w}_j^u(\alpha) + \hat{w}_j^\ell(\alpha)] = 2S_j^+(\alpha). \quad (40)$$

Solving (38) and (40) for  $\hat{w}_j^u(\alpha)$  and  $\hat{w}_j^\ell(\alpha)$ , we find that

$$\hat{w}_j(\alpha; y) = S_j^+(\alpha)/\gamma_j(\alpha) + \text{sgn}(y)T_j^+(\alpha). \quad (41)$$

Equation (38) can also be derived by applying a Fourier transform to the left-hand side of (37) and using [6, eqn. (1.74)]. However, attempting to obtain (40) in this way leads to technical problems, because the forward transform of  $\partial w_j/\partial y$  may not exist for  $x = 0$  (even with damping), due to the possibility of a nonintegrable singularity at the origin in the  $(x, y)$  plane.

Since  $\phi$  is subject to the same continuity conditions as  $w_j$ , we now have the Fourier representations

$$w_j(x, y) = \frac{1}{2\pi} \int_{\Gamma} \left[ \frac{S_j^+(\alpha)}{\gamma_j(\alpha)} + \text{sgn}(y)T_j^+(\alpha) \right] e^{-\gamma_j(\alpha)|y|} e^{-i\alpha x} d\alpha \quad (42)$$

and

$$\phi(x, y) = \frac{1}{2\pi} \int_{\Gamma} \left[ \frac{Q^+(\alpha)}{\gamma_3(\alpha)} + \text{sgn}(y)R^+(\alpha) \right] e^{-\gamma_3(\alpha)|y|} e^{-i\alpha x} d\alpha. \quad (43)$$

To prevent nonintegrable singularities at the origin in the  $(x, y)$  plane, we require that  $S_j^+(\alpha)/\gamma_j(\alpha)$ ,  $T_j^+(\alpha)$ ,  $Q^+(\alpha)/\gamma_3(\alpha)$  and  $R^+(\alpha)$  all tend to zero as  $\alpha \rightarrow \infty \in \Gamma$ . With these definitions,  $w_j$  and  $\phi$  satisfy the Helmholtz equation (with nondimensional wavenumber  $q_1$ ,  $q_2$  or  $q_3$  as appropriate), the Sommerfeld radiation condition and continuity conditions on  $y = 0$ ,  $x < 0$ . It remains to apply the boundary conditions on  $y = 0$ ,  $x > 0$  and to ensure that  $w$ ,  $\psi_x$  and  $\psi_y$  are bounded, so that the tip condition is fully satisfied.

## 5 Derivation of Wiener–Hopf equations

To determine the unknown functions in (42) and (43), we begin by applying the condition  $w^t(x, 0) = 0$ , for  $x > 0$ . The scattered contribution to  $w$  is obtained by simply adding  $w_1$  to  $w_2$ , so

$$w(x, y) = \frac{1}{2\pi} \int_{\Gamma} \left\{ \frac{S_1^+}{\gamma_1} e^{-\gamma_1|y|} + \frac{S_2^+}{\gamma_2} e^{-\gamma_2|y|} + \text{sgn}(y) \left[ T_1^+ e^{-\gamma_1|y|} + T_2^+ e^{-\gamma_2|y|} \right] \right\} e^{-i\alpha x} d\alpha. \quad (44)$$

Here we have omitted the argument  $\alpha$  from the functions  $S_j^+$ ,  $T_j^+$  and  $\gamma_j$  for brevity. To enable  $w$  to satisfy the boundary condition, cancelling the incident wave on both sides of the strip whilst remaining bounded, the antisymmetric term must disappear identically on  $y = 0$ . It is already known to be zero for  $y = 0$  and  $x < 0$ . For  $x > 0$  we require  $T_1^+(\alpha) + T_2^+(\alpha)$  to satisfy (32) in the *lower* half-plane. The only way to achieve this is

$$T_1^+(\alpha) = -T_2^+(\alpha) = T^+(\alpha), \quad (45)$$



say. To cancel the contribution from the incident wave (26) on the faces of the strip, we write

$$\frac{S_1^+(\alpha)}{\gamma_1(\alpha)} + \frac{S_2^+(\alpha)}{\gamma_2(\alpha)} = w^+(\alpha) + w^-(\alpha), \quad (46)$$

where

$$w^+(\alpha) = -i/(\alpha - \alpha_0), \quad \text{with} \quad \alpha_0 = -\cos \Theta. \quad (47)$$

The contour  $\Gamma$  must be indented to pass above the pole at  $\alpha = \alpha_0$ , so that the residue is included when  $y = 0$  and  $x > 0$ . Note that the contribution to  $w_j$  from the indentation around  $\alpha_0$  can be expressed in terms of the residue at the pole, according to [22, Corollary 5.8]. It does not violate the radiation condition, despite the fact that  $\text{Re}[\gamma_1(\alpha)] < 0$  on this section of the contour in cases where  $\cos \Theta < 0$  so that  $\alpha_0 > 0$ .

Further equations are now obtained from Fourier representations for the components of the in-plane rotation vector,  $\psi_x$  and  $\psi_y$ , defined in (8). Once again omitting the argument  $\alpha$  from  $\gamma_j$  and the unknown functions, we have

$$\begin{aligned} \psi_x(x, y) = & -\frac{1}{2\pi} \int_{\Gamma} \left[ i\alpha A_1 \frac{S_1^+}{\gamma_1} e^{-\gamma_1|y|} + i\alpha A_2 \frac{S_2^+}{\gamma_2} e^{-\gamma_2|y|} + R^+ \gamma_3 e^{-\gamma_3|y|} \right] e^{-i\alpha x} d\alpha \\ & - \frac{\text{sgn } y}{2\pi} \int_{\Gamma} \left[ (A_1 e^{-\gamma_1|y|} - A_2 e^{-\gamma_2|y|}) i\alpha T^+ + Q^+ e^{-\gamma_3|y|} \right] e^{-i\alpha x} d\alpha \end{aligned} \quad (48)$$

and

$$\begin{aligned} \psi_y(x, y) = & \frac{1}{2\pi} \int_{\Gamma} \left[ (A_2 \gamma_2 e^{-\gamma_2|y|} - A_1 \gamma_1 e^{-\gamma_1|y|}) T^+ + i\alpha \frac{Q^+}{\gamma_3} e^{-\gamma_3|y|} \right] e^{-i\alpha x} d\alpha \\ & - \frac{\text{sgn } y}{2\pi} \int_{\Gamma} \left[ A_1 S_1^+ e^{-\gamma_1|y|} + A_2 S_2^+ e^{-\gamma_2|y|} - i\alpha R^+ e^{-\gamma_3|y|} \right] e^{-i\alpha x} d\alpha. \end{aligned} \quad (49)$$

To eliminate the antisymmetric terms on  $y = 0$ , we require that

$$Q^+(\alpha) = i\alpha(A_2 - A_1)T^+(\alpha) \quad \text{and} \quad R^+(\alpha) = \frac{A_1 S_1^+(\alpha) + A_2 S_2^+(\alpha)}{i\alpha}. \quad (50)$$

Inserting the formula for  $R^+(\alpha)$  into (48) and setting  $y = 0$ , we find that

$$\psi_x(x, 0) = \frac{i}{2\pi} \int_{\Gamma} \left[ \left( \frac{\gamma_3}{\alpha} - \frac{\alpha}{\gamma_1} \right) A_1 S_1^+ + \left( \frac{\gamma_3}{\alpha} - \frac{\alpha}{\gamma_2} \right) A_2 S_2^+ \right] e^{-i\alpha x} d\alpha. \quad (51)$$

Then, by setting  $x > 0$  and deforming the contour  $\Gamma$  into the lower half-plane, we obtain

$$i \left( \frac{\gamma_3(\alpha)}{\alpha} - \frac{\alpha}{\gamma_1(\alpha)} \right) A_1 S_1^+(\alpha) + i \left( \frac{\gamma_3(\alpha)}{\alpha} - \frac{\alpha}{\gamma_2(\alpha)} \right) A_2 S_2^+(\alpha) = \psi_x^+(\alpha) + \psi_x^-(\alpha), \quad (52)$$

where

$$\psi_x^+(\alpha) = A_1 \cos \Theta / (\alpha - \alpha_0). \quad (53)$$

Now the residue from a pole at the origin does not depend on  $x$ , and therefore violates the boundary condition unless  $\Theta = \pi/2$ , in which case  $\alpha_0 = 0$ . However, if  $\alpha_0 = 0$  then  $\psi_x^+(\alpha) \equiv 0$ . Consequently, the functions  $S_j^+$  must be such that the singularity at the origin in (52) is removable. We will return to this matter in section 7. Finally, we must apply the boundary condition for  $\psi_y$ . From (49) and (50), we have

$$\psi_y(x, 0) = \frac{1}{2\pi} \int_{\Gamma} \left[ (A_2 \gamma_2 - A_1 \gamma_1) - (A_2 - A_1) \frac{\alpha^2}{\gamma_3} \right] T^+ e^{-i\alpha x} d\alpha, \quad (54)$$

meaning that

$$- \frac{T^+(\alpha)}{\gamma_3(\alpha)} K(\alpha) = \psi_y^+(\alpha) + \psi_y^-(\alpha), \quad (55)$$



where

$$\psi_y^+(\alpha) = A_1 \sin \Theta / (\alpha - \alpha_0) \quad (56)$$

and

$$K(\alpha) = A_1 \gamma_1(\alpha) \gamma_3(\alpha) - A_2 \gamma_2(\alpha) \gamma_3(\alpha) + (A_2 - A_1) \alpha^2. \quad (57)$$

Evidently, (55) is a scalar Wiener–Hopf equation; the factor  $-1/\gamma_3(\alpha)$  has been included so that

$$K(\alpha) \rightarrow K_\infty \quad \text{as} \quad \alpha \rightarrow \infty \in \Gamma, \quad (58)$$

where  $K_\infty > 0$ . A straightforward calculation shows that

$$K_\infty = [A_2(q_2^2 + q_3^2) - A_1(1 + q_3^2)]/2, \quad (59)$$

after which we use (9) and (25) followed by (11) to obtain

$$K_\infty = \frac{k_1^2 - k_2^2}{2k_1^2} \left( 1 + \frac{\kappa^2 k_s^2}{k_p^2} \right). \quad (60)$$

On the other hand, (52) must be used in conjunction with (46) to form a  $2 \times 2$  matrix Wiener–Hopf equation. Thus,

$$\mathbf{L}(\alpha) \begin{bmatrix} S_1^+(\alpha) \\ S_2^+(\alpha) \end{bmatrix} = \begin{bmatrix} w^+(\alpha) + w^-(\alpha) \\ \psi_x^+(\alpha) + \psi_x^-(\alpha) \end{bmatrix}, \quad (61)$$

where

$$\mathbf{L}(\alpha) = \begin{bmatrix} \frac{1}{\gamma_1(\alpha)} & \frac{1}{\gamma_2(\alpha)} \\ iA_1 \left( \frac{\gamma_3(\alpha)}{\alpha} - \frac{\alpha}{\gamma_1(\alpha)} \right) & iA_2 \left( \frac{\gamma_3(\alpha)}{\alpha} - \frac{\alpha}{\gamma_2(\alpha)} \right) \end{bmatrix}. \quad (62)$$

The determinant of this matrix kernel is given by

$$\det \mathbf{L}(\alpha) = - \frac{iK(\alpha)}{\alpha \gamma_1(\alpha) \gamma_2(\alpha)} \quad (63)$$

and the inverse by

$$\mathbf{L}^{-1}(\alpha) = \frac{1}{K(\alpha)} \begin{bmatrix} \gamma_1(\alpha) & 0 \\ 0 & \gamma_2(\alpha) \end{bmatrix} \begin{bmatrix} -A_2(\gamma_2(\alpha)\gamma_3(\alpha) - \alpha^2) & -i\alpha \\ A_1(\gamma_1(\alpha)\gamma_3(\alpha) - \alpha^2) & i\alpha \end{bmatrix}. \quad (64)$$

## 6 Solution to the scalar Wiener–Hopf equation

To solve (55), we must factorise  $K(\alpha)/\gamma_3(\alpha)$  into a product of functions that are analytic in  $\mathcal{D}^+$  or  $\mathcal{D}^-$ . The function  $\gamma_3$  can be factorised by inspection. Indeed,

$$\gamma_j^+(\alpha) = (-i(\alpha + q_j))_p^{1/2} \quad \text{and} \quad \gamma_j^-(\alpha) = (i(\alpha - q_j))_p^{1/2}, \quad j = 1, 2, 3, \quad (65)$$

where the subscript ‘ $p$ ’ denotes a principal value. These particular factors have been chosen so that  $\gamma_j^+(\alpha) = \gamma_j^-(-\alpha)$ . The branch cut of  $\gamma_j^+$  is located on the line  $\arg[\alpha + q_j] = -\pi/2$ , whereas the cut of  $\gamma_j^-$  lies on the line  $\arg[\alpha - q_j] = \pi/2$ . To factorise  $K(\alpha)$ , we use Cauchy integral formulae. Thus, from [6, section 1.3]

$$K^\pm(\alpha) = \sqrt{K_\infty} \exp \left[ \pm \frac{1}{2\pi i} \int_{\Gamma^\mp} \frac{\log[K(z)/K_\infty]}{z - \alpha} dz \right], \quad (66)$$

provided  $K$  is zero-free on the paths of integration. These are identical to the original contour  $\Gamma$  used in (30) except that  $\Gamma^+$  is indented to pass above the pole at  $z = \alpha$ , and  $\Gamma^-$  is indented to pass below. In principle, (66) can be evaluated by quadrature, but in practice its convergence is rather slow. A transformation into an integral suitable for numerical evaluation can be achieved by contour deformation, though there are some technical difficulties associated with this. The procedure is carried out in detail in the supplement.

Having obtained  $K^+$  and  $K^-$ , we rewrite (55) in the form

$$-\frac{T^+(\alpha)K^+(\alpha)}{\gamma_3^+(\alpha)} - \frac{\gamma_3^-(\alpha_0)}{K^-(\alpha_0)}\psi_y^+(\alpha) = \frac{\gamma_3^-(\alpha)\psi_y^-(\alpha)}{K^-(\alpha)} + \left(\frac{\gamma_3^-(\alpha)}{K^-(\alpha)} - \frac{\gamma_3^-(\alpha_0)}{K^-(\alpha_0)}\right)\psi_y^+(\alpha). \quad (67)$$

The left-hand side has no singularities in  $\mathcal{D}^+$ , and the right-hand side has no singularities in  $\mathcal{D}^-$ . Both sides are analytic on  $\Gamma$ , and therefore both must represent the same entire function,  $E(\alpha)$ , say. This can be determined as follows. First note that there can be no branch point at infinity, because branch points never occur individually. Next, observe that the factors  $K^\pm(\alpha)$  are expressed in terms of finite integrals in the supplement, and limits can be commuted with these; it follows from (S2) that  $K^\pm(\alpha) \rightarrow \sqrt{K_\infty}$  as  $\alpha \rightarrow \infty$  in any direction. Finally, since the unknown functions satisfy (32), it follows that there exists  $n_0 \in \mathbb{N}$  such that  $E(\alpha)/\alpha^{n_0} \rightarrow 0$  as  $\alpha \rightarrow \infty$  in any direction. By the extended form of Liouville's theorem,  $E(\alpha)$  must be a polynomial. However any polynomial other than the zero function will cause  $T^+(\alpha)$  and  $\psi^-(\alpha)$  to violate the tip condition. Hence  $E(\alpha) \equiv 0$ , so on returning to (67) we obtain

$$T^+(\alpha) = -\frac{\gamma_3^-(\alpha_0)\gamma_3^+(\alpha)}{K^-(\alpha_0)K^+(\alpha)}\psi_y^+(\alpha) \quad \text{and} \quad \psi_y^-(\alpha) = \left(\frac{\gamma_3^-(\alpha_0)K^-(\alpha)}{K^-(\alpha_0)\gamma_3^-(\alpha)} - 1\right)\psi_y^+(\alpha). \quad (68)$$

The function  $Q^+(\alpha)$  from (43) is now determined through its relationship to  $T^+(\alpha)$  (50). Note that  $\psi_y^+(\alpha) + \psi_y^-(\alpha) = O(\alpha^{-3/2})$  for large  $|\alpha|$ , meaning the integral in (54) remains convergent in the limit  $x \rightarrow 0$ , and therefore  $\psi_y(x, y)$  is bounded, in accordance with the tip condition.

## 7 Solution to the matrix Wiener–Hopf equation

The matrix equation (61) can be solved numerically by first expressing the unknowns in terms of functions that are analytic except for finite branch cuts. We begin by reconfiguring the complex plane so that now  $\alpha = 1$  is joined to  $\alpha = q_2$  by a straight branch cut and likewise  $\alpha = -1$  is joined to  $\alpha = -q_2$ ; see figure 2b. The cuts emanating from  $\alpha = \pm q_2$  and  $\alpha = \pm q_3$ , which run along the imaginary axis, are unchanged. Next, we observe that winding once around the three branch points at  $-1$ ,  $-q_2$  and  $-q_3$  causes the matrix kernel  $L(\alpha)$  in (61) to change sign, but leaves the right-hand side unchanged. Consequently,  $S_1^+$  and  $S_2^+$  must also change sign. There is some flexibility in the means by which this is achieved; we might try introducing factors of  $\gamma_j^+(\alpha)$  for  $j = 1, 2$  or  $3$  to either the numerator or denominator of  $S_j^+(\alpha)$ . Since the implicit quadrature method described in appendix A allows unknown functions to possess square root singularities, a correct solution can be obtained even if the wrong factor is introduced at this stage. However, we must ensure that the construction does not create spurious poles. For example if we assume that an unknown function has a factor  $\gamma_j^\pm(\alpha)$  in the numerator when in fact this should appear in the denominator, then a correct solution would require the implicit quadrature method to numerically generate a pole at  $\alpha = \mp q_j$ , which is not possible.

Now there can be no factor  $\gamma_j^+(\alpha)$  in the denominator of  $S_j^+(\alpha)$ , because this would create a pole at  $\alpha = -q_j$  in the Fourier representation for  $w_j$  (42). The residue from such a pole does not depend on  $y$ , and such a contribution to the scattered field is unphysical. Therefore we may write

$$S_j^+(\alpha) = \left(\tilde{S}_j^+(\alpha) + \frac{c_j}{\alpha - \alpha_0}\right)\gamma_j^+(\alpha), \quad (69)$$

where we have introduced the convention that a function with the accent ‘ $\sim$ ’ has no branch point at infinity. The second term in the brackets has been included because there must be simple poles at  $\alpha = \alpha_0$  on the left-hand side of (61), to match the poles of  $w^+$  and  $\psi_x^+$ . The constants  $c_1$  and  $c_2$  can be determined by equating residues; thus

$$L(\alpha_0) \begin{bmatrix} \gamma_1^+(\alpha_0) & 0 \\ 0 & \gamma_2^+(\alpha_0) \end{bmatrix} \begin{bmatrix} c_1 \\ c_2 \end{bmatrix} = - \begin{bmatrix} i \\ A_1\alpha_0 \end{bmatrix}. \quad (70)$$

Then, using the inverse matrix (64) yields

$$c_1 = \frac{i\gamma_1^-(\alpha_0)}{K(\alpha_0)} [A_2\gamma_2(\alpha_0)\gamma_3(\alpha_0) + (A_1 - A_2)\alpha_0^2] \quad (71)$$

and

$$c_2 = -\frac{iA_1}{K(\alpha_0)} \gamma_2^-(\alpha_0) \gamma_1(\alpha_0) \gamma_3(\alpha_0). \quad (72)$$

We must also set conditions so that the singularity at the origin in the lower row of the Wiener–Hopf equation (which comes from (52)) is removable. In general, imposing the condition

$$A_1 \tilde{S}_1^+(0) \gamma_1^+(0) + A_2 \tilde{S}_2^+(0) \gamma_2^+(0) = \frac{A_1 c_1 \gamma_1^+(0) + A_2 c_2 \gamma_2^+(0)}{\alpha_0}, \quad (73)$$

removes the pole, but this cannot be used directly if  $\alpha_0 = 0$ . However, using (71) and (72), it is not difficult to show that the numerator on the right-hand side of (73) vanishes in the limit  $\alpha_0 \rightarrow 0$ . To resolve the limit, we write

$$\frac{A_1 c_1 \gamma_1^+(0) + A_2 c_2 \gamma_2^+(0)}{\alpha_0} = \frac{b_1 + b_2 \alpha_0 + b_3 \alpha_0^2}{K(\alpha_0)} + O(\alpha_0^3), \quad (74)$$

and expand  $K(\alpha_0)c_1$  and  $K(\alpha_0)c_2$  about  $\alpha_0 = 0$  using the series

$$\gamma_j(\alpha_0) = -iq_j + \frac{i\alpha_0^2}{2q_j} + O(\alpha_0^4) \quad \text{and} \quad \gamma_j^-(\alpha_0) = \gamma_j^-(0)P(\alpha_0/q_j) + O(\alpha_0^4), \quad (75)$$

where

$$P(z) = 1 - \frac{z}{2} - \frac{z^2}{8} - \frac{z^3}{16}. \quad (76)$$

A simple calculation with a computer algebra package then shows that

$$b_1 = \frac{A_1 A_2}{2} q_3 (q_2 - 1), \quad b_2 = A_1^2 - A_1 A_2 \left[ 1 + \frac{3q_3}{8} \left( q_2 - \frac{1}{q_2} \right) \right] \quad (77)$$

and

$$b_3 = -\frac{A_1^2}{2} + \frac{A_1 A_2}{2} \left[ 1 + \frac{1}{2} \left( \frac{1 - q_2}{q_3} + q_3 - \frac{q_3}{q_2} \right) + \frac{q_3}{8} \left( q_2 - \frac{1}{q_2^2} \right) \right]. \quad (78)$$

The right-hand side of (73) can now be evaluated for small  $|\alpha_0|$  using (74).

We must also eliminate the infinite branch cut in the upper half-plane from the Wiener–Hopf equation (61). As it stands, the left-hand side changes sign when  $\alpha$  winds once around the three points 1,  $q_2$  and  $q_3$ , and we can match this behaviour by introducing a factor of  $\gamma_j^-(\alpha)$  to each row on the right-hand side. To avoid the possibility of creating spurious poles, we place these factors in the denominators, writing

$$w^+(\alpha) + w^-(\alpha) = \frac{\tilde{w}^-(\alpha)/\gamma_1^-(\alpha)}{\alpha - \alpha_0} \quad \text{and} \quad \psi_x^+(\alpha) + \psi_x^-(\alpha) = \frac{\tilde{\psi}_x^-(\alpha)/\gamma_2^-(\alpha)}{\alpha - \alpha_0}. \quad (79)$$

The values of the unknown functions at  $\alpha = \alpha_0$  can be deduced by matching residues; thus

$$\tilde{w}^-(\alpha_0) = -i\gamma_1^-(\alpha_0) \quad \text{and} \quad \tilde{\psi}_x^-(\alpha_0) = -A_1 \alpha_0 \gamma_2^-(\alpha_0). \quad (80)$$

Returning to (61), we now have

$$\mathbf{M}(\alpha) \begin{bmatrix} (\alpha - \alpha_0) \tilde{S}_1^+(\alpha) + c_1 \\ (\alpha - \alpha_0) \tilde{S}_2^+(\alpha) + c_2 \end{bmatrix} = \begin{bmatrix} \tilde{w}^-(\alpha) \\ \tilde{\psi}_x^-(\alpha) \end{bmatrix}, \quad (81)$$

where

$$\mathbf{M}(\alpha) = \begin{bmatrix} \gamma_1^-(\alpha) & 0 \\ 0 & \gamma_2^-(\alpha) \end{bmatrix} \mathbf{L}(\alpha) \begin{bmatrix} \gamma_1^+(\alpha) & 0 \\ 0 & \gamma_2^+(\alpha) \end{bmatrix} \quad (82)$$

$$= \begin{bmatrix} 1 & \frac{\gamma_1^-(\alpha)}{\gamma_2^-(\alpha)} \\ \frac{iA_1 \gamma_2^-(\alpha)}{\alpha \gamma_1^-(\alpha)} (\gamma_1(\alpha) \gamma_3(\alpha) - \alpha^2) & \frac{iA_2}{\alpha} (\gamma_2(\alpha) \gamma_3(\alpha) - \alpha^2) \end{bmatrix}. \quad (83)$$

Note that (63) and (82) immediately give the determinant as

$$\det \mathbf{M}(\alpha) = \gamma_1(\alpha)\gamma(\alpha)_2 \det \mathbf{L}(\alpha) = -iK(\alpha)/\alpha \quad (84)$$

Next let us consider the behaviour of the functions  $\tilde{S}_j^+(\alpha)$ ,  $\tilde{w}^-(\alpha)$  and  $\tilde{\psi}_x^-(\alpha)$  as  $\alpha \rightarrow \infty$ . Since  $S_j^+(\alpha)$  satisfies (32) in  $\mathcal{D}^+$ , it follows from (69) and (81) that there exists  $n_1 \in \mathbb{N}$  such that  $\tilde{w}^-(\alpha)/\alpha^{n_1}$  and  $\tilde{\psi}_x^-(\alpha)/\alpha^{n_1}$  both tend to zero as  $\alpha \rightarrow \infty \in \mathcal{D}^+$ . Since  $\tilde{w}^-(\alpha)$  and  $\tilde{\psi}_x^-(\alpha)$  satisfy (32) in  $\mathcal{D}^-$ , neither can possess an essential singularity at infinity. Finally, since there is no branch point at infinity, the behaviour of these functions as  $\alpha \rightarrow \infty$  cannot depend on direction. From (44), (46) and (79), if  $\tilde{w}^-(\alpha)$  is  $O(\alpha^n)$  as  $\alpha \rightarrow \infty$  then  $w$  will be unbounded in the vicinity of the origin, violating the tip condition. We can deduce that  $\tilde{\psi}_x^-(\alpha)$  remains bounded as  $\alpha \rightarrow \infty$  in the same way. Therefore we may write

$$w_\infty = \lim_{\alpha \rightarrow \infty} \tilde{w}^-(\alpha) \quad \text{and} \quad \psi_{x,\infty} = \lim_{\alpha \rightarrow \infty} \tilde{\psi}_x^-(\alpha). \quad (85)$$

By similar reasoning, we can show that the behaviour of  $\tilde{S}_j^+(\alpha)$  as  $\alpha \rightarrow \infty$  is the same in every direction. Consequently,  $\tilde{S}_j^+(\alpha)$  must remain bounded as  $\alpha \rightarrow \infty$ , or else  $S_j^+(\alpha)/\gamma_j(\alpha)$  is also unbounded, leading to a nonintegrable singularity at the origin in  $w_j$  (see (42)), which is forbidden. A constant contribution to  $\tilde{S}_1^+(\alpha)$  produces an unbounded term in  $w_1$ , and if such a term exists it must cancel a corresponding term in  $w_2$ . Therefore it must be the case that as  $\alpha \rightarrow \infty$ ,

$$\tilde{S}_1^+(\alpha) \rightarrow -\tilde{S}_2^+(\alpha) \rightarrow S_\infty, \quad (86)$$

say, so that the transverse displacement  $w = w_1 + w_2$  is bounded. A relationship between  $\psi_{x,\infty}$  and  $S_\infty$  can be determined by multiplying (61) by  $\mathbf{L}^{-1}$ , taking the limit  $\alpha \rightarrow \infty$  and retaining only leading-order terms. In this way, we find that

$$\psi_{x,\infty} = iK_\infty S_\infty. \quad (87)$$

Despite considerable effort, we have not been able to find a similar result for  $w_\infty$ .

The implicit quadrature method from appendix A can be applied to (81). The unknowns are

$$\mathbf{f}^+(\alpha) = \begin{bmatrix} \tilde{S}_1^+(\alpha) \\ \tilde{S}_2^+(\alpha) \end{bmatrix}, \quad \mathbf{g}^-(\alpha) = \begin{bmatrix} \tilde{w}^-(\alpha) \\ \tilde{\psi}_x^-(\alpha) \end{bmatrix}, \quad \mathbf{f}_\infty = \begin{bmatrix} S_\infty \\ -S_\infty \end{bmatrix} \quad \text{and} \quad \mathbf{g}_\infty = \begin{bmatrix} w_\infty \\ iK_\infty S_\infty \end{bmatrix} \quad (88)$$

and the coefficients are

$$\mathbf{A}(\alpha) = (\alpha - \alpha_0)\mathbf{M}(\alpha), \quad \mathbf{B}(\alpha) \equiv \begin{bmatrix} -1 & 0 \\ 0 & -1 \end{bmatrix} \quad \text{and} \quad \mathbf{C}(\alpha) = -\mathbf{M}(\alpha) \begin{bmatrix} c_1 \\ c_2 \end{bmatrix}. \quad (89)$$

Since  $\mathbf{B}(\alpha)$  is entire, the products  $\mathbf{B}_\ell \mathbf{B}_r^{-1}$  disappear from (A117). Also, in view of (84), zeros of  $\det \mathbf{M}(\alpha)$  coincide with zeros of the scalar kernel  $K(\alpha)$ . Now  $K(\alpha)$  is zero free on the primary sheet of the Riemann surface if the cuts are those used for the factorisation of the scalar kernel in the supplement. However, these cuts are not suitable for use with the implicit quadrature method because they pass close to each other in the neighbourhood of the origin. Using straight line cuts from  $\pm 1$  to  $\pm q_2$  changes the value of  $\gamma_1$  within the regions bounded by the triangles  $(0, 1, q_2)$  and  $(0, -1, -q_2)$ , so that  $\det \mathbf{A}(\alpha)$  may have zeros on the right face of the cut in the lower half-plane, but not on the left face (compare figure 2b to figure S1a in the supplement). Consequently, we use the alternative form of (A118), with the subscripts  $\ell$  and  $r$  interchanged, and  $\Delta \mathbf{F}_p$  replaced by  $-\Delta \mathbf{F}_p$ . This equation can be simplified using the fact that  $\mathbf{A}_r \mathbf{A}_\ell^{-1} \mathbf{C}_\ell = \mathbf{C}_r$ , which means the right-hand side is identically zero.

Of the various constants appearing in (88) and (89),  $c_1$  and  $c_2$  have already been determined, and the presence of  $S_\infty$  can be countered by including (73) in the system of equations, with the right-hand side evaluated using (74) if necessary. The presence of the additional constant  $w_\infty$  means the process of matching values at quadrature nodes does not fully determine  $\mathbf{f}^+(\alpha)$  and  $\mathbf{g}^-(\alpha)$ . To close the system, we can equate the two sides of one row from the Wiener–Hopf equation at one additional point. A natural choice is the first row at the origin. Hence, we require that

$$\gamma_2^-(0)[c_1 - \alpha_0 \tilde{S}_1^+(0)] + \gamma_1^-(0)[c_2 - \alpha_0 \tilde{S}_2^+(0)] = \gamma_2^-(0)\tilde{w}^-(0). \quad (90)$$

The relations (80) will now be satisfied automatically, since  $\mathbf{f}^+(\alpha)$  and  $\mathbf{g}^-(\alpha)$  are uniquely determined. These can be used as a check on the correctness of the numerical code, because they are not directly included in the linear system formed from (A110). Some technical details of the implementation used to solve (81) are provided in the supplement.

## 8 The low frequency limit

In the limit  $\omega \rightarrow 0$ , Mindlin's model reduces to the classical (Kirchhoff) plate theory, and we can recover the results of [11]. Some differences in notation must be taken into account:  $\gamma_1$  and  $\gamma_2$  here are represented by  $\lambda$  and  $\gamma$ , respectively in [11], and the opposite sign convention for Fourier integrals is used (compare (42) to [11, eqn. (2.3)]). The leading-order behaviour at low frequencies is obtained by setting  $k_s = k_p = 0$ , in which case the Helmholtz equations for  $w_1$  and  $w_2$  are equivalent to the governing equation for a Kirchhoff plate. We then have  $k_2^2 = -k_1^2$  from (10) so that  $q_2 = i$ . Also, (11) shows that  $|q_3| \rightarrow \infty$  as  $\omega \rightarrow 0$  because  $k_s = O(\omega)$  whereas  $k_2 = O(\sqrt{\omega})$ . For the boundary conditions we observe that  $A_2 \rightarrow A_1 \rightarrow -1$  as  $\omega \rightarrow 0$  (see (9)), so (8) reduces to

$$\psi_x = -\frac{\partial w}{\partial x} + \frac{\partial \phi}{\partial y} \quad \text{and} \quad \psi_y = -\frac{\partial w}{\partial y} - \frac{\partial \phi}{\partial x}. \quad (91)$$

Since the total transverse displacement  $w^t$  vanishes on the rigid strip, it follows immediately that  $\partial w^t / \partial x = 0$  here as well. Therefore the leading-order contributions to  $\psi_x^t$  and  $\psi_y^t$  vanish on the rigid strip if  $\phi(x, y) = 0$  for all  $x$  and all  $y$  and  $\partial w^t / \partial y = 0$  for  $y = 0$  and  $x > 0$ . Thus we retrieve the conditions for Kirchhoff theory. The scalar Wiener–Hopf equation (55) reduces to

$$-\frac{T^+(\alpha)}{\gamma_2(\alpha)} K_c(\alpha) = \psi_y^+(\alpha) + \psi_y^-(\alpha), \quad \text{with} \quad K_c(\alpha) = \gamma_2(\alpha)[\gamma_2(\alpha) - \gamma_1(\alpha)]. \quad (92)$$

Multiplying the numerator and denominator on the right-hand side by  $\gamma_2(\alpha) + \gamma_1(\alpha)$  recovers the antisymmetric case considered in [11]. Note that  $K_c(\alpha)$  has no branch point at infinity and that  $K_c(\alpha) \rightarrow 1$  as  $\alpha \rightarrow \infty$ . After setting  $A_1 = A_2 = -1$  in the matrix kernel (62), (61) can be reduced to a single equation by observing that the choice

$$S_2^+(\alpha) = -S_1^+(\alpha) \quad (93)$$

eliminates terms involving  $\gamma_3$ . The second row is then a scalar multiple of the first, and corresponds to requiring that  $\partial w^t / \partial x = 0$  on the rigid strip. The first row of (61) becomes

$$L_c(\alpha) S_1^+(\alpha) = w^+(\alpha) + w^-(\alpha) \quad \text{with} \quad L_c(\alpha) = \frac{1}{\gamma_1(\alpha)} - \frac{1}{\gamma_2(\alpha)}. \quad (94)$$

This is equivalent to the symmetric problem in [11]. A factorisation of  $L_c(\alpha)$  can be obtained from the factorisation of  $K_c(\alpha)$  because  $[\gamma_2(\alpha)]^2 \gamma_1(\alpha) L_c(\alpha) = K_c(\alpha)$ . Finally, note that using (93) in (46) shows that

$$\alpha^2 [w^+(\alpha) + w^-(\alpha)] \rightarrow 0 \quad \text{as} \quad \alpha \rightarrow \infty \in \Gamma, \quad (95)$$

since  $S_j(\alpha)/\alpha \rightarrow 0$  in this limit. This is to be expected — with  $\phi$  absent from (8) and  $A_2 = A_1$ , the physical requirement that  $\psi_x$  and  $\psi_y$  must be bounded reduces to requiring that first derivatives of  $w$  are bounded, which is guaranteed by (95). Another consequence of (95) is that second derivatives of  $w$  are  $O(r^\eta)$  with  $\eta > -1$  in the vicinity of the origin, so a product of two is integrable (in the two-dimensional sense). This shows that the approach taken in [11], the effect of which is to require that each individual term in the strain energy density is integrable, is correct. However, it should be noted that the authors of [11] assume slightly more than is actually necessary (see their equations (2.6)–(2.8)): the strain energy density certainly is integrable if  $\eta \geq -1/2$  (and in fact the final results show that  $\eta = -1/2$ ), but  $\eta > -1$  is a sufficient condition.

## 9 The far field displacement

To determine the far field pattern, we begin by calculating contributions from the pole at  $\alpha = \alpha_0$  in the integral representation (42). These are not present at all locations, but the reflection coefficients will appear in the analysis below. Now (69) shows that the residue of  $S_j^+$  is  $c_j \gamma_j^+(\alpha_0)$ , and the values for  $c_j$  are given by (71)–(72). From (68) and (56), we obtain

$$\text{Res}_{\alpha=\alpha_0} T^+(\alpha) = -i A_1 \gamma_1(\alpha_0) \gamma_3(\alpha_0) / K(\alpha_0), \quad (96)$$

having used the fact that  $\sin \Theta = i\gamma_1(\alpha_0)$ . For  $y > 0$ , the residue contribution to  $w_1$  cancels the incident field, whereas the contribution to  $w_2$  evaluates to zero, meaning the singularity at  $\alpha = \alpha_0$  is removable in this case. For  $y < 0$ , the residues represent the reflected field. We find that

$$w_j^r = \mathcal{R}_j e^{ix \cos \Theta + y \gamma_j(\cos \Theta)}, \quad j = 1, 2, \quad (97)$$

with amplitude coefficients given by

$$\mathcal{R}_1 = -\overline{K}(\cos \Theta)/K(\cos \Theta) \quad \text{and} \quad \mathcal{R}_2 = -2i \operatorname{Im}[K(\cos \Theta)]/K(\cos \Theta), \quad (98)$$

where the overbar denotes a complex conjugate. Note that  $|\mathcal{R}_1| = 1$ , which is to be expected on physical grounds. Also, the total contribution from the residue terms and the incident field satisfies the boundary conditions on the rigid strip, so  $\mathcal{R}_1 + \mathcal{R}_2 + 1 = 0$ .

Next, we write  $(x, y) = r(\cos \theta, \sin \theta)$  and apply the method of steepest descents [23, Chapter 3] to (42) for large  $r$ , with the branch cuts returned to their original configuration from figure 2a. For the integral with  $\gamma_j$  in the exponent, we find a simple saddle point at  $\alpha = -q_j \cos \theta$ , and

$$\gamma_j(-q_j \cos \theta) |\sin \theta| - i q_j \cos^2 \theta = -i q_j. \quad (99)$$

The effect of deforming the contour of integration onto the steepest descents paths is considered in the supplement. It turns out that  $w_2$  does not contribute to the diffracted field at leading order, except near the boundary and then only at grazing incidence ( $\Theta \approx 0$ ). For  $w_1$ , a basic saddle point analysis (ignoring the pole at  $\alpha = \alpha_0$ ) produces the approximation

$$w_1^d(r, \theta, \Theta) = \frac{e^{ir} e^{i\pi/4}}{\sqrt{2\pi r}} d(\theta, \Theta) + O(r^{-3/2}), \quad (100)$$

where the diffraction coefficient is given by

$$d(\theta, \Theta) = S_1^+(-\cos \theta) - i \sin \theta T^+(-\cos \theta). \quad (101)$$

Using (68), (56), (69) and (71) this becomes

$$\begin{aligned} d(\theta, \Theta) = & \tilde{S}_1^+(-\cos \theta) \gamma_1^-(\cos \theta) - \frac{i}{2s^- s^+} \left[ \frac{A_1 \gamma_3^+(\cos \Theta) \gamma_3^-(\cos \theta)}{K^+(\cos \Theta) K^-(\cos \theta)} \sin \Theta \sin \theta \right. \\ & \left. + \frac{\gamma_1^+(\cos \Theta) \gamma_1^-(\cos \theta)}{K(\cos \Theta)} [A_2 \gamma_2(\cos \Theta) \gamma_3(\cos \Theta) + (A_1 - A_2) \cos^2 \Theta] \right], \end{aligned} \quad (102)$$

where

$$s^\pm = \sin\left(\frac{\Theta}{2} \pm \frac{\theta}{2}\right), \quad (103)$$

and we have simplified using the fact that  $\gamma_j^+(-\alpha) = \gamma_j^-(\alpha)$  and likewise for  $K^\pm(\alpha)$ . It follows from the reduced matrix Wiener–Hopf equation (81) and (84) that  $\tilde{S}_1^+(\alpha)$  remains bounded in the limit  $\alpha \rightarrow -1$ , provided  $\alpha_0 \neq -1$ . Consequently,  $d(0, \Theta) = d(2\pi, \Theta) = 0$ , provided  $\Theta \neq 0$ .

The approximation (100) breaks down in the vicinity of the shadow and reflection boundaries at  $\theta = \Theta$  and  $\theta = 2\pi - \Theta$ , respectively. Mathematically, this is due to the pole at  $\alpha = \alpha_0$ ; physically it corresponds to the Fresnel (or penumbra) regions [4, Chapter 5], across which the contribution from either the incident or reflected field rapidly but continuously becomes visible as  $\theta$  is increased. A uniform approximation which takes the pole into account and remains valid in the Fresnel regions follows immediately from [24, eqn. (2.25)]. Thus,

$$\begin{aligned} w_1^t(r, \theta, \Theta) = & \frac{e^{ir}}{2} \left\{ \frac{e^{i\pi/4}}{\sqrt{2\pi r}} \left[ 2d(\theta, \Theta) - \frac{1}{s^-} - \frac{\mathcal{R}_1}{s^+} \right] \right. \\ & \left. + \operatorname{erfs}(\sqrt{2r} e^{i\pi/4} s^-) + \mathcal{R}_1 \operatorname{erfs}(\sqrt{2r} e^{i\pi/4} s^+) \right\} + O(r^{-3/2}), \end{aligned} \quad (104)$$



where the term in square brackets remains bounded in the limits  $s^\pm \rightarrow 0$  and  $\text{erfs}(\cdot)$  represents the scaled complex error function (usually denoted by  $w$ ); that is

$$\text{erfs}(z) = e^{-z^2} \text{erfc}(-iz). \quad (105)$$

Note that (104) is an approximation to the total field, whereas (100) includes the diffracted component only and also that the terms in (104) involving scaled complex error functions are exact solutions to the Helmholtz equation. If  $s^+$  or  $s^-$  is negative, a plane wave term can be extracted from (104) using the identity [25, eqn. (7.4.3)]

$$\text{erfs}(z) = 2e^{-z^2} - \text{erfs}(-z). \quad (106)$$

A uniform approximation for the diffracted field only is therefore given by

$$w_1^d(r, \theta, \Theta) = \frac{e^{ir}}{2} \left\{ \frac{e^{i\pi/4}}{\sqrt{2\pi r}} \left[ 2d(\theta, \Theta) - \frac{1}{s^-} - \frac{\mathcal{R}_1}{s^+} \right] + \text{sgn}(s^-) \text{erfs}(\sqrt{2r} e^{i\pi/4} |s^-|) + \mathcal{R}_1 \text{sgn}(s^+) \text{erfs}(\sqrt{2r} e^{i\pi/4} |s^+|) \right\} + O(r^{-3/2}). \quad (107)$$

If neither  $|s^+|$  nor  $|s^-|$  is close to zero, the asymptotic formula formula [25, eqn. (7.12.1)]

$$\text{erfs}(z) \sim \frac{i}{z\sqrt{\pi}}, \quad -\frac{\pi}{4} < \arg z < \frac{5\pi}{4} \quad (108)$$

can be used to retrieve (100) from (107). In the special case  $\Theta = 0$  (head-on incidence), one should always take  $\text{sgn}(s^-) = -1$  and  $\text{sgn}(s^+) = 1$ , including at  $\theta = 0$  and  $\theta = 2\pi$ . This represents the fact that the incident field is present everywhere whereas there is no reflected field at all. Therefore, in order to obtain the diffracted component of the field in this case, (106) must always be applied to the first error function in (104), but never the second. Another way to view this is that if  $\Theta$  is small but nonzero, then  $s^- > 0$  in the limit  $\theta \rightarrow 0$ , but if  $\Theta = 0$  exactly zero then  $s^- < 0$  in the same limit (and similarly for  $s^+$  as  $\theta \rightarrow 2\pi$ ).

Let us now consider the behaviour of the uniform approximation on the rigid strip. For nonzero  $\Theta$ , setting  $\theta = 0$  in (104), we find that

$$w_1^t(r, 0, \Theta) = 2A_1 \cos\left(\frac{\Theta}{2}\right) \frac{\gamma_3(\cos \Theta)}{K(\cos \Theta)} e^{ir} \left\{ \frac{e^{-i\pi/4}}{\sqrt{2\pi r}} + i \sin\left(\frac{\Theta}{2}\right) \text{erfs}(\sqrt{2r} e^{i\pi/4} \sin \frac{\Theta}{2}) \right\} + O(r^{-3/2}), \quad (109)$$

having used (98) and (57) to write the reflection coefficient explicitly. If  $\Theta$  is such that (108) can be applied then the  $O(r^{-1/2})$  terms cancel. However, this fails at grazing incidence. We can obtain a similar result for  $\theta = 2\pi$ ; the main difference in that case is the extra contribution  $-\mathcal{R}_2 e^{ir \cos \Theta}$ , which cancels the residue term from  $w_2$ . In summary, the uniform approximation is bounded, correctly includes the incident and reflected waves, and also the Fresnel type terms that capture the behaviour of the field as the shadow and reflection boundaries are crossed. It also includes the correct  $O(r^{-1/2})$  term except near the boundary at grazing incidence, when the rigid strip lies inside the Fresnel regions. A conflicting remark concerning the Kirchhoff analogue of (104) between equations (3.5) and (3.6) of [24] is incorrect: the  $O(r^{-1/2})$  term does *not* vanish on the boundary if  $\Theta = 0$ ; one cannot set  $c = 1$  and  $\theta = 0$  simultaneously in (2.21) of [24].

Figures 3–5 show how the diffracted field varies with  $\theta$ . The parameter  $r$ , representing the nondimensional distance from the tip of the rigid strip to the observer (i.e. the actual distance multiplied by  $k_1$ ; see (23)) is fixed at 100. The solid curves show the results for Kirchhoff theory. The only variables remaining in this model are  $\theta$  and  $\Theta$ . The length scaling (23) removes  $k_1$ , and there is no dependence on the Poisson ratio because the boundary conditions reduce to  $w^t = \partial w^t / \partial y = 0$  (see section 8). For the Mindlin model, the Poisson ratio used is  $\nu = 0.26$ , which is the approximate value for steel, and the shear correction factor  $\kappa$  is set at  $\pi/\sqrt{12}$ , which is one possible value suggested by Mindlin [14] (see also [18, section 8.3.1]). According to (29), the frequency at which  $k_1 = \pi/h$  corresponds to  $\omega^* \approx 2.59$ . Note that the symbols on the curves for  $\omega^* = 0.5, 1.0$  and  $2.5$  are an aid to visual distinction only; the actual number of data points used to create each curve is approximately 1000.



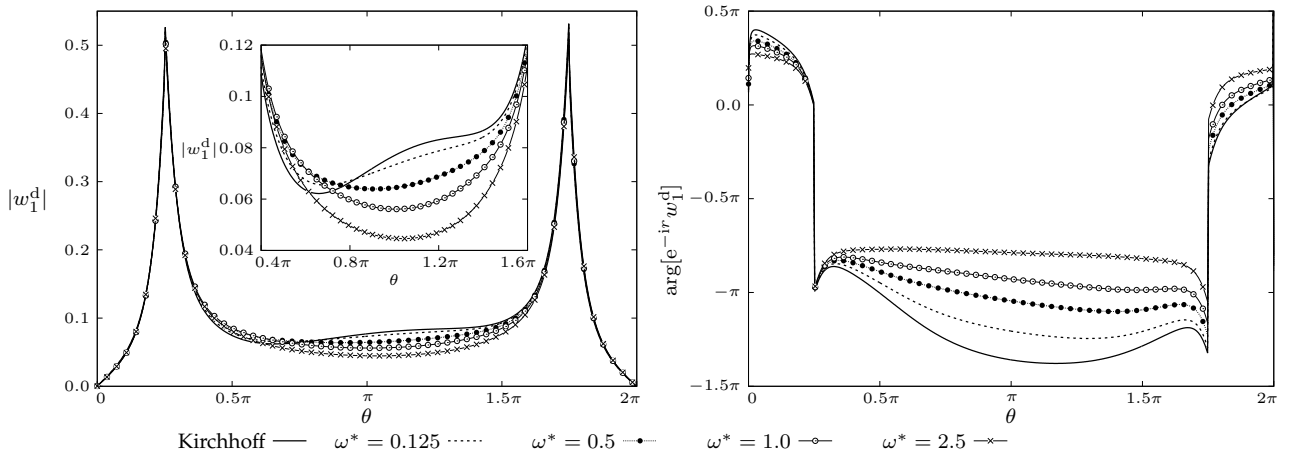


Figure 3: Modulus and phase of the uniform approximation to the far field diffraction pattern, with  $\Theta = \pi/4$ . The nondimensional distance from the origin to the observation point is fixed at 100.

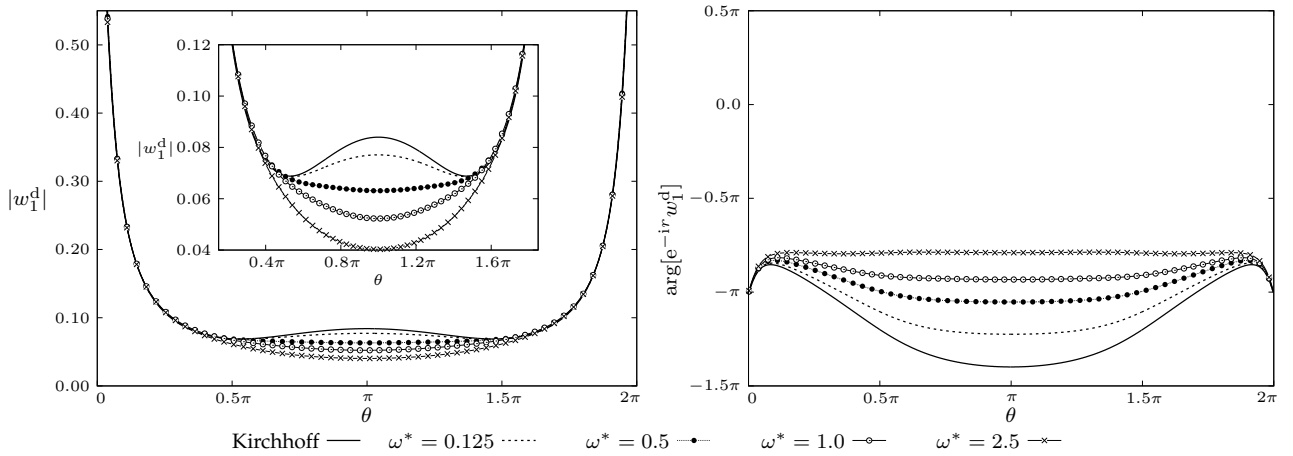


Figure 4: Modulus and phase of the uniform approximation to the far field diffraction pattern, with  $\Theta = 0$ . The nondimensional distance from the origin to the observation point is fixed at 100.

In figure 3, the angle of incidence is  $\pi/4$ , and the peaks in the diffracted field at the shadow and reflection boundaries are clearly evident. The modulus of  $w_1^d$  has only small discontinuities at these points because  $\text{erfs}(0) = 1$ , whereas all other terms in (107) are  $O(1/\sqrt{r})$ . For the same reason, the magnitude of the discontinuities in the argument of  $e^{-ir}w_1^d$  is approximately  $\pi$ . In the vicinity of the shadow and reflection boundaries, the results from Kirchhoff theory are in close agreement with Mindlin theory, and there is very little variation as the frequency is increased. This is because the first error function term in (107) is determined by the incident field alone, and does not depend on  $\omega^*$ . The second error function term depends on  $\omega^*$  through the reflection coefficient  $\mathcal{R}_1$ , which always has unit modulus (see (98)). For Kirchhoff theory, the phase of  $\mathcal{R}_1$  is  $2\pi/3$ . For Mindlin theory the phase increases with  $\omega^*$ ; the value for  $\omega^* = 2.5$  is approximately  $0.927\pi$ . In the region where the incident field is present but the reflected field is not (i.e. between the two peaks), the strength of the diffracted field decreases as  $\omega^*$  is increased, except near the shadow boundary, where it initially increases. As expected, the overall behaviour exhibited at higher frequencies is quite different to the predictions from Kirchhoff theory.

Figure 4 shows the leading order diffracted field at head-on incidence, i.e.  $\Theta = 0$ . In this case,  $e^{-ir}w_1^d \approx -1$  for  $\theta = 0$  and  $\theta = 2\pi$  because the diffracted field cancels the incident wave on the faces of the strip; there is no specular reflection. Outside the Fresnel regions, the decrease in the diffracted field as  $\omega^*$  increases is again visible. Finally, figure 5 shows the diffracted field at normal incidence, that is  $\Theta = \pi/2$ . In this case, the space between the Fresnel regions is narrow, and there is relatively little variation of  $|w_1^d|$  with frequency. Consequently, Kirchhoff theory predicts the magnitude of the

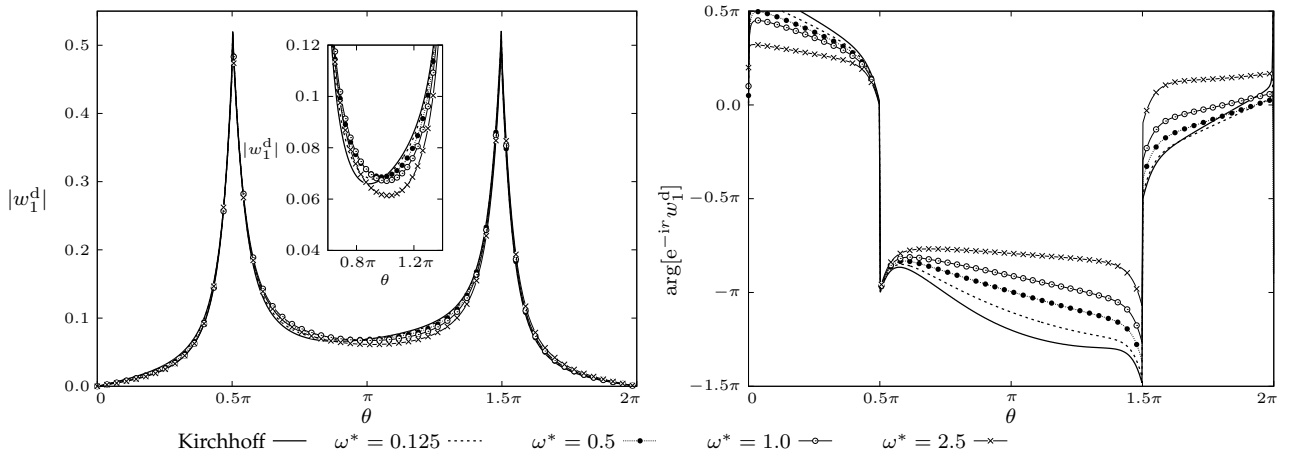


Figure 5: Modulus and phase of the uniform approximation to the far field diffraction pattern, with  $\Theta = \pi/2$ . The nondimensional distance from the origin to the observation point is fixed at 100.

diffracted field rather well in this case, though there are significant deviations in the phase.

## 10 Concluding remarks

The effect of diffraction by a rigid strip in a plate modelled by Mindlin theory has been determined, and the results compared to predictions from the simpler Kirchhoff theory. As one might expect, Kirchhoff theory performs well at low frequencies, but is inaccurate at higher frequencies. Diffraction by a crack will be the subject of a future paper. This is a more challenging problem because the field excites motion along the edges of the crack, and the boundary conditions (corresponding to zero shear force, bending moment and twisting moment) are much more complicated than those for a rigid strip (zero displacement). In addition, diffraction at a crack tip excites the localised ‘edge waves’ discovered in [19]. These propagate along the faces of the crack and decay exponentially in the perpendicular direction; their existence gives rise to poles in the Wiener–Hopf kernel [11, 12]. An outline solution to the crack diffraction problem is contained in [9], but no results are presented.<sup>2</sup>

The implicit quadrature method used to solve the matrix Wiener–Hopf equation has a number of attractive features. It directly determines the unknown functions, without the need for a kernel factorisation, and can be applied to complicated equations with no particular difficulty. In those cases where a matrix Wiener–Hopf equation can be solved ‘exactly,’ evaluation of the kernel factors typically requires one or more quadrature calculations at each point in the complex plane (see e.g. [17]). This is similar to the case of scalar factorisations such as (66). The implicit quadrature method generates Cauchy integral representations for the unknown functions, and these can be used throughout the complex plane. Evaluating one of these representations at a point requires a quadrature calculation. Thus the added cost of the implicit quadrature method amounts to the formation and solution of the relevant linear system of algebraic equations. This is a small price to pay for the ability to solve matrix Wiener–Hopf equations of arbitrary complexity, especially in view of the fact that only one such system is required for each set of parameters (frequency, angle of incidence, Poisson ratio, etc.). Further improvements to the implicit quadrature method may be possible by designing a more sophisticated algorithm to position the nodes.

The author would like to thank the Isaac Newton Institute for Mathematical Sciences, Cambridge, for support and hospitality during the programme *Bringing pure and applied analysis together via the Wiener–Hopf technique, its generalisations and applications* where work on this paper was undertaken. This work was supported by EPSRC grant no EP/R014604/1.

<sup>2</sup>The outline solution ends with a reference to an unpublished article; see earlier footnote on page 1.

## References

- [1] Hellier C. 2003 *Handbook of Nondestructive Evaluation*. New York: McGraw-Hill.
- [2] Schmerr LW. 2016 *Fundamentals of Ultrasonic Nondestructive Evaluation*. Switzerland: Springer second edition.
- [3] Achenbach JD, Gautesen AK, McMaken H. 1982 *Ray Methods for Waves in Elastic Solids: with Applications to Scattering by Cracks*. Boston: Pitman.
- [4] Borovikov VA, Kinber BY. 1994 *Geometrical theory of diffraction*. London: Institute of Electrical Engineers.
- [5] Sommerfeld AJW. 1896 Mathematische Theorie der Diffraction. *Mathematische Annalen* **47**, 317–374.
- [6] Noble B. 1988 *Methods Based on the Wiener–Hopf Technique*. Chelsea.
- [7] Bouwkamp CJ. 1953 Diffraction theory. *Rep. Prog. Phys.* **17**, 35–100.
- [8] Achenbach JD, Gautesen AK. 1977 Geometrical Theory of Diffraction for 3-D Elastodynamics. *J. Acoust. Soc. Am.* **61**, 413–421.
- [9] Abrahams ID. 2002 On the application of the Wiener–Hopf technique to problems in dynamic elasticity. *Wave Motion* **36**, 311–333.
- [10] Emets VS, Rogowski J. 2016 Two-dimensional elastodynamic scattering by a finite flat crack. *J. Appl. Mech.* **83**.
- [11] Norris AN, Wang Z. 1994 Bending-wave diffraction from strips and cracks on thin plates. *Q. J. Mech. Appl. Math.* **47**, 607–627.
- [12] Thompson I, Abrahams ID. 2005 Diffraction of flexural waves by cracks in orthotropic thin elastic plates. I Formal solution. *Proc. Roy. Soc. Lond., A* **461**, 3413–3434.
- [13] Thompson I, Abrahams ID. 2007 Diffraction of flexural waves by cracks in orthotropic thin elastic plates. Part II. Far field analysis. *Proc. Roy. Soc. Lond., A* **463**, 1615–1638.
- [14] Mindlin RD. 1951 Influence of rotatory inertia and shear on flexural motion of isotropic, elastic plates. *J. Appl. Mech.* **18**, 31–38.
- [15] Mindlin RD, Yang J. 2006 *An Introduction to the Mathematical Theory of Vibrations of Elastic Plates*. Singapore: World Scientific.
- [16] Khrapkov AA. 1971 Certain cases of the elastic equilibrium of an infinite wedge with a nonsymmetric notch at the vertex, subjected to concentrated forces. *Appl. Math. Mech. (PMM)* **35**, 625–637.
- [17] Abrahams ID. 1998 On the non-commutative factorization of Wiener–Hopf kernels of Khrapkov type. *Proc. Roy. Soc. Lond., A* **454**, 1719–1743.
- [18] Graff KF. 1991 *Wave Motion in Elastic Solids*. New York: Dover.
- [19] Norris AN, Krylov VV, Abrahams ID. 2000 Flexural edge waves and Comments on “A new bending wave solution for the classical plate equation” [J. Acoust. Soc. Am. 104, 2220–2222 (1998)]. *J. Acoust. Soc. Am.* **107**, 1781–1784.
- [20] Vemula C, Norris AN. 1997 Flexural wave propagation and scattering on thin plates using Mindlin theory. *Wave Motion* **26**, 1–12.
- [21] Achenbach JD. 1973 *Wave Propagation in Elastic Solids*. North-Holland.

- [22] Osborne AD. 1999 *Complex Variables and their Applications*. Harlow, UK: Addison–Wesley.
- [23] Murray JD. 1984 *Asymptotic Analysis*. New York: Springer-Verlag.
- [24] Thompson I. 2006 An improved uniform approximation for diffraction integrals. *Proc. Roy. Soc. Lond., A* **462**, 1341–1353.
- [25] Olver FWJ, Lozier DW, Boisvert RF, Clark CW. 2010 *NIST Handbook of Mathematical Functions*. Cambridge, UK: Cambridge University Press.

## A Implicit quadrature method

Consider a matrix Wiener–Hopf equation of the form

$$\mathbf{A}(\alpha)\mathbf{f}^+(\alpha) + \mathbf{B}(\alpha)\mathbf{g}^-(\alpha) = \mathbf{C}(\alpha), \quad (\text{A110})$$

where the only singularities of the unknown vector functions  $\mathbf{f}^+(\alpha)$  and  $\mathbf{g}^-(\alpha)$  are finite branch cuts in the lower and upper half-plane, respectively. Let  $\Omega^-$  and  $\Omega^+$  be anticlockwise oriented contours encircling the branch cuts in the lower and upper half-planes, respectively; see figure A1. Suppose that  $\mathbf{f}^+(\alpha) \rightarrow \mathbf{f}_\infty$  and  $\mathbf{g}^-(\alpha) \rightarrow \mathbf{g}_\infty$  as  $\alpha \rightarrow \infty$  (it is possible to allow unbounded behaviour by replacing  $\mathbf{f}_\infty$  and  $\mathbf{g}_\infty$  with entire functions, but this is not necessary here). Then, if  $\alpha$  is a point outside  $\Omega^\pm$ , we have

$$\mathbf{f}^+(\alpha) = \mathbf{f}_\infty - \frac{1}{2\pi i} \int_{\Omega^-} \frac{\mathbf{f}^+(z)}{z - \alpha} dz \quad \text{and} \quad \mathbf{g}^-(\alpha) = \mathbf{g}_\infty - \frac{1}{2\pi i} \int_{\Omega^+} \frac{\mathbf{g}^-(z)}{z - \alpha} dz. \quad (\text{A111})$$

These formulae can be verified by expanding the integration contours, collecting the residues at  $z = \alpha$ , writing  $z = Me^{i\theta}$  and then letting  $M \rightarrow \infty$ . The coefficients  $\mathbf{A}(\alpha)$  and  $\mathbf{B}(\alpha)$  are assumed to be matrices, though one may in fact be scalar, leading to some slight simplifications. At this point, the shapes of  $\Omega^+$  and  $\Omega^-$  are somewhat arbitrary, but it turns out to be convenient to wrap the contours tightly around the branch cuts (see figure A1). For simplicity in the text below, we will present the details of the method for the case where there are two cuts: one each in the upper and lower half-planes, both with identifiable left and right faces. Subscripts ‘ $\ell$ ’ and ‘ $r$ ’ will be used to denote function values on the faces, and we will also use a subscript ‘ $s$ ’ to mean either ‘ $\ell$ ’ or ‘ $r$ ’. For a horizontal cut one may replace right and left with upper and lower, respectively. The method generalises immediately to cases with multiple cuts, though care must be taken to determine on which face of a cut (if any) a zero of  $\det \mathbf{A}(\alpha)$  or  $\det \mathbf{B}(\alpha)$  may occur.

Suppose now that the integrals in (A111) are evaluated by quadrature, using nodes  $z_j^+$  and  $z_j^-$ , distributed along the branch cuts in the upper and lower half-planes, respectively. Then

$$\mathbf{f}^+(\alpha) = \mathbf{f}_\infty - \frac{1}{2\pi i} \sum_{j=1}^{n_-} \frac{V_j^-(\mathbf{F}_{j,r} - \mathbf{F}_{j,\ell})}{z_j^- - \alpha} \quad \text{and} \quad \mathbf{g}^-(\alpha) = \mathbf{g}_\infty - \frac{1}{2\pi i} \sum_{j=1}^{n_+} \frac{V_j^+(\mathbf{G}_{j,r} - \mathbf{G}_{j,\ell})}{z_j^+ - \alpha}, \quad (\text{A112})$$

where  $V_j^\pm$  are the quadrature weights, and

$$\mathbf{F}_{j,s} = \mathbf{f}_s^+(z_j^-) \quad \text{and} \quad \mathbf{G}_{j,s} = \mathbf{g}_s^-(z_j^+). \quad (\text{A113})$$

We have allowed different numbers of nodes in the upper and lower half-planes in (A112) because the functions  $\mathbf{f}^+(\alpha)$  and  $\mathbf{g}^-(\alpha)$  may be rather different in nature. Evaluating (A110) at  $z = z_p^+$  yields

$$\mathbf{B}_s(z_p^+)\mathbf{G}_{p,s} + \mathbf{A}_s(z_p^+) \left[ \mathbf{f}_\infty - \frac{1}{2\pi i} \sum_{j=1}^{n_-} \frac{V_j^-(\mathbf{F}_{j,r} - \mathbf{F}_{j,\ell})}{z_j^- - z_p^+} \right] = \mathbf{C}_s(z_p^+), \quad p = 1, \dots, n_+, \quad (\text{A114})$$

whereas evaluating at  $z = z_p^-$  yields

$$\mathbf{A}_s(z_p^-)\mathbf{F}_{p,s} + \mathbf{B}_s(z_p^-) \left[ \mathbf{g}_\infty - \frac{1}{2\pi i} \sum_{j=1}^{n_+} \frac{V_j^+(\mathbf{G}_{j,r} - \mathbf{G}_{j,\ell})}{z_j^+ - z_p^-} \right] = \mathbf{C}_s(z_p^-), \quad p = 1, \dots, n_-. \quad (\text{A115})$$

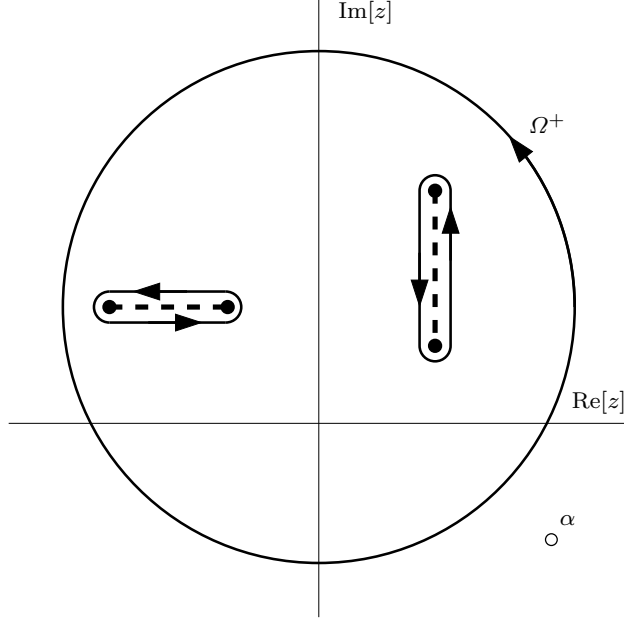


Figure A1: The contour  $\Omega^+$  encircling the branch cuts in the upper half-plane, and the ‘collapsed’ version, wrapped tightly around the branch cuts.

Each of these provides two equations ( $s = \ell$  and  $s = r$ ) for every row in the Wiener–Hopf equation. Further simplifications can often be achieved by exploiting the fact that computing  $\mathbf{f}^+(\alpha)$  and  $\mathbf{g}^-(\alpha)$  using (A112) requires only the differences between the right and left values, and not the values themselves. Therefore we define new unknowns

$$\Delta \mathbf{F}_j = V_j^-(\mathbf{F}_{j,r} - \mathbf{F}_{j,\ell}) \quad \text{and} \quad \Delta \mathbf{G}_j = V_j^+(\mathbf{G}_{j,r} - \mathbf{G}_{j,\ell}), \quad (\text{A116})$$

and solve for these directly. Provided  $\det \mathbf{B}(\alpha)$  has no zeros on the right face of the cut in the upper half-plane, we may multiply the ‘ $r$ ’ version of (A114) by  $\mathbf{B}_\ell(z_p^+) \mathbf{B}_r^{-1}(z_p^+)$  and then subtract the ‘ $\ell$ ’ version to obtain

$$\begin{aligned} \mathbf{B}_\ell(z_p^+) \Delta \mathbf{G}_p + V_p^+ \left[ \mathbf{B}_\ell(z_p^+) \mathbf{B}_r^{-1}(z_p^+) \mathbf{A}_r(z_p^+) - \mathbf{A}_\ell(z_p^+) \right] \left[ \mathbf{f}_\infty - \frac{1}{2\pi i} \sum_{j=1}^{n_-} \frac{\Delta \mathbf{F}_j}{z_j^- - z_p^+} \right] \\ = V_p^+ \left[ \mathbf{B}_\ell(z_p^+) \mathbf{B}_r^{-1}(z_p^+) \mathbf{C}_r(z_p^+) - \mathbf{C}_\ell(z_p^+) \right], \quad p = 1, 2, \dots, n_+. \end{aligned} \quad (\text{A117})$$

If instead  $\det \mathbf{B}(\alpha)$  has no zeros on the left face of the cut, then we obtain the same equation but with  $\Delta \mathbf{G}_p$  replaced by  $-\Delta \mathbf{G}_p$  and  $\ell$  and  $r$  interchanged throughout. If  $\mathbf{B}_\ell(\alpha)$  and  $\mathbf{B}_r(\alpha)$  are commutative (e.g. if  $\mathbf{B}(\alpha)$  is a diagonal matrix), then the constraint regarding zeros can be dropped; in this case (A117) can be formally multiplied by  $\mathbf{B}_r(z_p^-)$  and simplified accordingly. The second part of the linear system (A115) can be treated in exactly the same way. Provided  $\det \mathbf{A}(\alpha)$  is zero free on the right face of the branch cut in the lower half-plane, we find that

$$\begin{aligned} \mathbf{A}_\ell(z_p^-) \Delta \mathbf{F}_p + V_p^- \left[ \mathbf{A}_\ell(z_p^-) \mathbf{A}_r^{-1}(z_p^-) \mathbf{B}_r(z_p^-) - \mathbf{B}_\ell(z_p^-) \right] \left[ \mathbf{g}_\infty - \frac{1}{2\pi i} \sum_{j=1}^{n_+} \frac{\Delta \mathbf{G}_j}{z_j^+ - z_p^-} \right] \\ = V_p^- \left[ \mathbf{A}_\ell(z_p^-) \mathbf{A}_r^{-1}(z_p^-) \mathbf{C}_r(z_p^-) - \mathbf{C}_\ell(z_p^-) \right], \quad p = 1, 2, \dots, n_-. \end{aligned} \quad (\text{A118})$$

The indices  $\ell$  and  $r$  can be interchanged provided  $\Delta \mathbf{F}_p$  is replaced by  $-\Delta \mathbf{F}_p$ ; this produces an alternative form of (A118) which is valid if  $\det \mathbf{A}(\alpha)$  has no zeros on the left face of the cut. The constraint on zeros can be dropped following multiplication by  $\mathbf{A}_r(z_p^-)$  if  $\mathbf{A}_\ell(\alpha)$  and  $\mathbf{A}_r(\alpha)$  are commutative.

The system formed from (A117) and (A118) (or (A114) and (A115)) can be solved numerically, provided additional information is included to account for the presence of  $\mathbf{f}_\infty$  and  $\mathbf{g}_\infty$ . It may be

possible to obtain values for these constants directly; otherwise augmenting equations (such as (73)) can be included in the linear system. If no further information regarding  $\mathbf{f}^+(\alpha)$  and  $\mathbf{g}^-(\alpha)$  can be obtained analytically, we choose a point  $\beta$  (or several points  $\beta_p$ ) at which both  $\mathbf{f}^+$  and  $\mathbf{g}^-$  can be computed by quadrature (i.e.  $\beta$  must not lie on or near the faces of the branch cuts) and close the system by enforcing equality in (A110) at this point. That is,

$$\mathbf{A}(\beta) \left[ \mathbf{f}_\infty - \frac{1}{2\pi i} \sum_{j=1}^{n_-} \frac{\Delta \mathbf{F}_j}{z_j^- - \beta} \right] + \mathbf{B}(\beta) \left[ \mathbf{g}_\infty - \frac{1}{2\pi i} \sum_{j=1}^{n_+} \frac{\Delta \mathbf{G}_j}{z_j^+ - \beta} \right] = \mathbf{C}(\beta). \quad (\text{A119})$$

A final issue concerns the quadrature to be used when evaluating the integrals in (A111). The locations of the nodes and the values of the weights must be adjusted to account for the possibility of square root singularities on the path of integration. A simple approach is to divide each branch cut into line sections in such a way that a singularity can occur at one end of each line section at most. Suppose that  $L$  is a straight line section along the right face of a branch cut, starting at the point  $a$  and ending at  $b$ , and consider the integral

$$\mathbf{J} = \int_L [h_r(z) - h_\ell(z)] dz, \quad (\text{A120})$$

where  $h(z)$  has a square root singularity at  $z = a$ . Then we simply write  $s^2 = z - a$  to obtain

$$\mathbf{J} = 2 \int_0^{(b-a)^{1/2}} [h_r(s^2 + a) - h_\ell(s^2 + a)] s ds. \quad (\text{A121})$$

Since the integrand is an odd function of  $s$ , the sign taken for  $(b-a)^{1/2}$  is unimportant. If we now apply a quadrature in the  $s$  plane, using nodes  $s_j$  and weights  $V_j$ , we obtain

$$\mathbf{J} \approx 2 \sum_{j=1}^n s_j V_j [h_r(s_j^2 + a) - h_\ell(s_j^2 + a)]. \quad (\text{A122})$$

Thus the nodes in the  $z$  plane are given by  $s_j^2 + a$ , and the weights by  $2s_j V_j$ . By applying quadrature in this way, the effect of the singularity at  $z = a$  is eliminated, because the function  $sh(s^2 + a)$  is analytic at  $s = 0$ . The situation in which the singularity appears at  $z = b$  can be handled in the same way. In the context of numerically solving Wiener–Hopf equations, these transformations are very convenient because the weights are ‘absorbed’ into the unknown coefficients via (A116). If the integrand is unbounded in the vicinity of a square root singularity, the coefficients  $\Delta \mathbf{F}_j$  and  $\Delta \mathbf{G}_j$  remain bounded due to the influence of the factor  $s_j$ .

# Supplementary material for ‘Diffraction by a rigid strip in a plate modelled by Mindlin theory’

Ian Thompson\*,

Department of Mathematical Sciences, University of Liverpool,  
Liverpool L69 7ZL, UK

November 6, 2020

## S1 Factorisation of the scalar kernel

To transform the kernel factorisation integral (66) into a form useful for numerical computation, it is necessary to deform the paths of integration. Zeros of  $K(\alpha)$  could interfere with this process, but we can rule these out as follows. First, from (57), we observe that  $K(0) = -|q_3|(A_2|q_2| + iA_1)$ , which is clearly nonzero. Hence there exists  $\epsilon > 0$  such that  $K(\alpha) \neq 0$  for  $|\alpha| < \epsilon$ . Next, we reposition the branch cuts emanating from  $\pm 1$  to run along the real and imaginary axes, joining 1 to  $q_2$  and  $-1$  to  $-q_2$ . Near the origin, we use curved indentations that lie inside the circle  $|\alpha| < \epsilon$ . Since the multivalued components of  $K(\alpha)$  are the products  $\gamma_1\gamma_3$  and  $\gamma_2\gamma_3$ , neither of which has a branch point at infinity, the cuts above  $q_3$  and below  $-q_3$  now disappear, and the new configuration is as shown in figure S1a. The paths of integration ( $\Gamma^\pm$  in (66)) can pass between the curved sections of the cuts, so that their orientation with respect to all of the branch points is preserved.

We may now use the principle of the argument [1, section 7.3] to prove that  $K$  is zero-free on the primary sheet of the Riemann surface. We begin by observing that (58) now holds as  $\alpha \rightarrow \infty$  in any direction, because we are using finite branch cuts. Consequently,  $\log[K(\alpha)]$  will return to its original value if  $\alpha$  traverses a circle of radius  $N$ , centred at the origin, provided  $N$  is sufficiently large. To complete the proof, it is sufficient to show that  $K(\alpha)$  cannot be real and negative on the faces of the branch cuts. It then follows  $\log[K(\alpha)]$  remains unchanged after  $\alpha$  encircles the branch cuts, because there can be no winding around the origin in the  $K$  plane. For  $\alpha = v$  and  $\alpha = iq_2v$  with  $-1 < v < 1$ ,  $\gamma_1$  is strictly negative imaginary whereas all other terms in  $K$  are real. Therefore  $K(\alpha)$  cannot be real here. The remaining sections of the cuts can be handled in a similar way, making use of the inequalities (15).

Next, we observe that  $K$  is an even function, so it follows from (66) that  $K^+(\alpha) = K^-(-\alpha)$ . Since we also have the relationship  $K(\alpha) = K^+(\alpha)K^-(\alpha)$ , it is sufficient to determine  $K^-(\alpha)$  in the region  $\text{Re}[\alpha] < -\text{Im}[\alpha]$ . To achieve this, we deform the contour  $\Gamma^+$  upwards. Letting  $\epsilon \rightarrow 0$  leaves an integral along the faces of the ‘L’ shaped cut in the upper half-plane, which we denote by  $\Gamma'$ . This consists of straight lines from  $\alpha = 1$  to the origin and then to  $\alpha = q_3$  (see figure S1b). Then (66) becomes

$$K^-(\alpha) = \sqrt{K_\infty} \exp \left[ \frac{1}{2\pi i} \int_{\Gamma'} \left\{ \log \left( \frac{K_\ell(z)}{K_\infty} \right) - \log \left( \frac{K_r(z)}{K_\infty} \right) \right\} \frac{dz}{z - \alpha} \right], \quad (\text{S1})$$

where the subscripts ‘ $\ell$ ’ and ‘ $r$ ’ refer to evaluation on the left and right faces of the cut, respectively. Note that  $\Gamma^+$  in (66) is traversed from left to right, and passes below the ‘L’ shaped cut, whereas  $\Gamma'$  is traversed from right to left, so that a factor  $-1$  is introduced to the term involving  $K_\ell$ . Since  $K(z)/K_\infty$  cannot be negative real on the faces of the cuts, we may take principal values for both logarithms. On the left face of the cut, values of the functions  $\gamma_j$  are unchanged from the original configuration in figure 2a in the main body of the paper. Therefore  $\gamma_1\gamma_3$  is negative imaginary, whereas  $\gamma_2\gamma_3$  may be

---

\*ian.thompson@liv.ac.uk



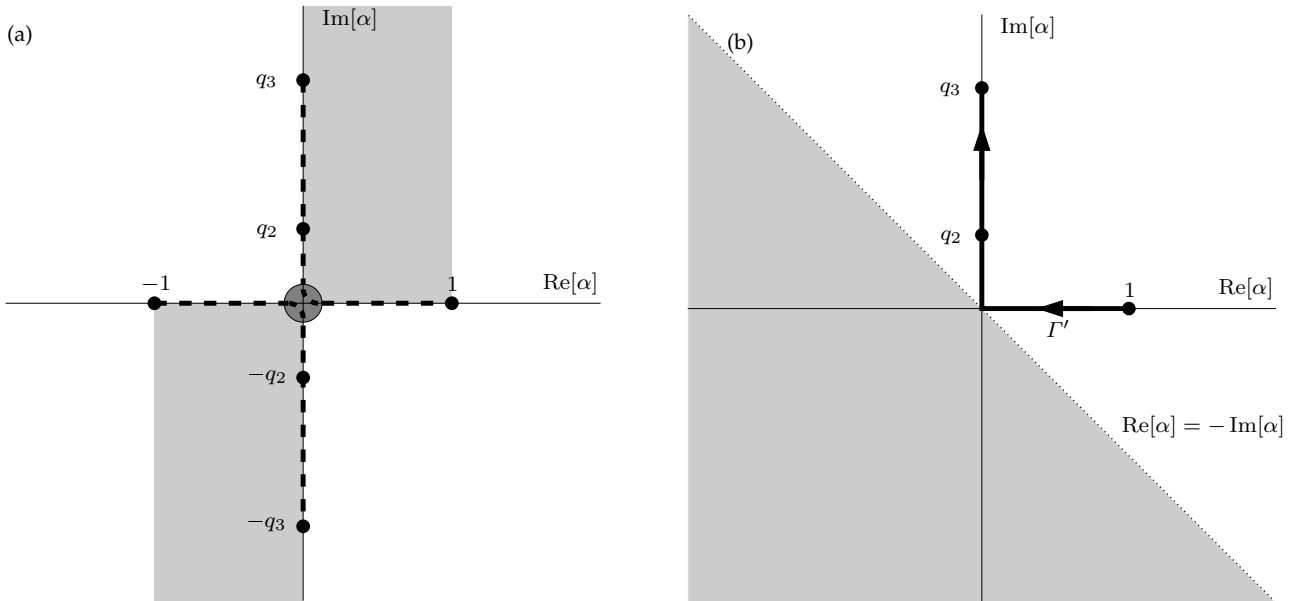


Figure S1: (a) Adjusted branch cuts chosen such that scalar kernel is zero free. The shaded rectangular regions show where  $K(\alpha)$  differs from its value in the original configuration in figure 2a in the main body of the paper. The radius of the dark circle ( $\epsilon$ ) is such that  $K(\alpha) \neq 0$  for  $|\alpha| < \epsilon$ . (b) The contour  $\Gamma'$  used in computing the scalar kernel factors. The variable  $\alpha$  lies in the shaded grey region.

positive real or negative imaginary. On the right face of the cut, the real terms are unchanged but the imaginary terms switch sign, so that  $K_r(z) = \overline{K}_\ell(z)$ . Therefore,

$$K^-(\alpha) = \sqrt{K_\infty} \exp \left[ \frac{1}{\pi} \int_{\Gamma'} \arg[K_\ell(z)] \frac{dz}{z - \alpha} \right], \quad (\text{S2})$$

where the argument is a principal value.

Finally, we address the fact that  $\alpha$  may lie close to the integration contour. Since there are no branch points at  $\alpha = \pm q_3$  in the Kirchhoff problem (see section 8), we also cause the contribution from the path joining  $q_2$  to  $q_3$  to disappear as  $\omega \rightarrow 0$ . We begin by splitting  $\Gamma'$  into two parts:  $\Gamma'_1$  joining  $\alpha = 1$  to the origin and then to  $q_2$ , and  $\Gamma'_2$  joining  $q_2$  to  $q_3$ . Now (S2) is only used for values of  $\alpha$  on or to the left of the line  $\text{Re}[\alpha] = -\text{Im}[\alpha]$ . Therefore, for the purpose of numerical integration,  $\alpha$  may lie close to  $\Gamma'_1$  but not to  $\Gamma'_2$ . Also, since  $A_j \rightarrow -1$  as  $\omega \rightarrow 0$ , it follows from (57) that  $K_\ell(z)$ , the value of the scalar kernel on the left face of the branch cut, is positive imaginary for  $z \in \Gamma'_2$  in the low frequency limit. Next, we write

$$\int_{\Gamma'} \arg[K_\ell(z)] \frac{dz}{z - \alpha} = \int_{\Gamma'_1} \left( \arg[K_\ell(z)] - \arg[K(\alpha)] \right) \frac{dz}{z - \alpha} + \int_{\Gamma'_2} \left( \arg[K_\ell(z)] - \frac{\pi}{2} \right) \frac{dz}{z - \alpha} + H(\alpha), \quad (\text{S3})$$

where

$$H(\alpha) = \arg[K(\alpha)] \int_{\Gamma'_1} \frac{dz}{z - \alpha} + \frac{\pi}{2} \int_{\Gamma'_2} \frac{dz}{z - \alpha} \quad (\text{S4})$$

$$= \arg[K(\alpha)] \log\left(\frac{\alpha - q_2}{\alpha - 1}\right) + \frac{\pi}{2} \log\left(\frac{\alpha - q_3}{\alpha - q_2}\right). \quad (\text{S5})$$

Since the variation in the argument of  $z - \alpha$  cannot exceed  $\pi$  as  $z$  traverses either contour in (S4), both logarithms in the last expression are principal values. The remaining integrals in (S3) are suitable for numerical evaluation. The implementation used to produce the numerical results in the main body of the paper employs mappings as in (A120)–(A122) to remove end-point square root singularities, and

applies the seven point Gaussian quadrature rule with adaptive refinement. In this way, the kernel factors are computed to near machine precision. Note that the second integral vanishes from (S3) as  $\omega \rightarrow 0$ , and the last term produces a factor  $(\alpha - q_3)^{1/2}(\alpha - q_2)^{-1/2}$  in  $K^-(\alpha)$  so that the branch points at  $\pm q_3$  disappear from the Wiener–Hopf equation in this limit.

## S2 Implementation of the implicit quadrature method

The main obstacle to numerically evaluating the solution to the matrix problem discussed in section 7 of the main paper relates to the location of nodes for use in the implicit quadrature scheme. Choosing the nodes a priori leads to a simple implementation but does not control errors in an efficient way. Instead, we use an adaptive scheme that works as follows. First, the integration contours are each divided into four sections, using the vertices

$$\pm 1, \quad \pm(1 + q_2)/2, \quad \pm q_2, \quad \pm(q_2 + q_3)/2 \quad \text{and} \quad \pm q_3. \quad (\text{S6})$$

The end-point singularities are removed using (A120)–(A122). A small set of nodes is then generated by applying a single step of a quadrature rule to each integral in the  $s$  plane. A second set of nodes is generated by applying the same quadrature rule in two equal steps. The resulting linear systems are solved, and contributions to  $\tilde{S}_j^+(\alpha)$ ,  $\tilde{w}^-(\alpha)$  and  $\tilde{\psi}_x^-(\alpha)$  from each section are calculated for a set of test points. Errors in the initial estimates can be computed using the second set of nodes, since these produce more accurate results. Nodes on subintervals for which the results meet a specified tolerance are retained, and subintervals on which the errors are too large are bisected again. This process is repeated until all results satisfy the tolerance condition. Using code written in Fortran 2003, running at double precision and configured to use the seven point Gaussian rule, a linear system sufficient to provide results accurate to ten significant figures was formed and solved in under 30 seconds on a six core machine running at 3GHz. Typically the number of nodes required was around one thousand. Almost all of the CPU time was used in solving the necessary linear systems; the CPU time used by other components of the implementation is very small in comparison.

Having applied the implicit quadrature method, the functions  $\tilde{S}_j^+(\alpha)$ ,  $\tilde{w}^-(\alpha)$  and  $\tilde{\psi}_x^-(\alpha)$  can be evaluated using their Cauchy integral representations. A useful test at this stage is to compute both sides of the Wiener–Hopf equation (81) and compare their values. We can also make use of (81) to avoid the situation in which quadrature becomes inaccurate due to branch cut proximity. The strategy is similar to the use of the identity  $K^+(\alpha) = K^-(-\alpha)$  in the scalar problem, above. We begin by dividing the plane across the line  $\mathcal{L} : \text{Im } \alpha = -|q_2| \text{Re } \alpha$ . On and to the right of  $\mathcal{L}$ , we compute  $\tilde{S}_j^+(\alpha)$  directly by quadrature. To the left of the line  $\mathcal{L}$ , we compute  $\tilde{w}^-(\alpha)$  and  $\tilde{\psi}_x^-(\alpha)$  by quadrature. It follows from (84) that the removable singularity disappears from (81) upon multiplication by  $M^{-1}$ . Therefore we may compute  $\tilde{S}_j^+(\alpha)$  from  $\tilde{w}^-(\alpha)$  and  $\tilde{\psi}_x^-(\alpha)$ , including near the origin. If  $\alpha \approx \alpha_0$  then (viewed as an equation for determining  $\tilde{S}_j^+(\alpha)$ ), (81) is subject to cancellation. In most cases this issue can be avoided by simply computing  $\tilde{S}_j^+(\alpha)$  directly by quadrature. Both methods for computing  $\tilde{S}_j^+(\alpha)$  may be inaccurate if  $\alpha_0 \approx -1$  and  $\alpha \approx \alpha_0$  simultaneously. In practice this is unimportant because the cancellation in (81) leads to a magnification of error roughly proportional to  $(\alpha - \alpha_0)^{-1}$ , which does not cause all precision to be lost. This issue can be avoided entirely by using (79) and (64) in (61) to obtain

$$S_1^+(\alpha) = \frac{-\gamma_1^+(\alpha)}{(\alpha - \alpha_0)K(\alpha)} \left[ A_2(\gamma_2(\alpha)\gamma_3(\alpha) - \alpha^2)\tilde{w}^-(\alpha) + \frac{i\alpha\gamma_1^-(\alpha)\tilde{\psi}_x^-(\alpha)}{\gamma_2^-(\alpha)} \right], \quad (\text{S7})$$

after which the diffraction coefficient can be evaluated using (101).

## S3 Steepest descents analysis

To apply the method of steepest descents to the diffraction integral (42), it is necessary to consider the effects that singularities may have on the process of deforming the integration contour. Writing

$$\gamma_j(\alpha)|\sin \theta| + i\alpha \cos \theta = -iq_j + v, \quad v \geq 0, \quad (\text{S8})$$

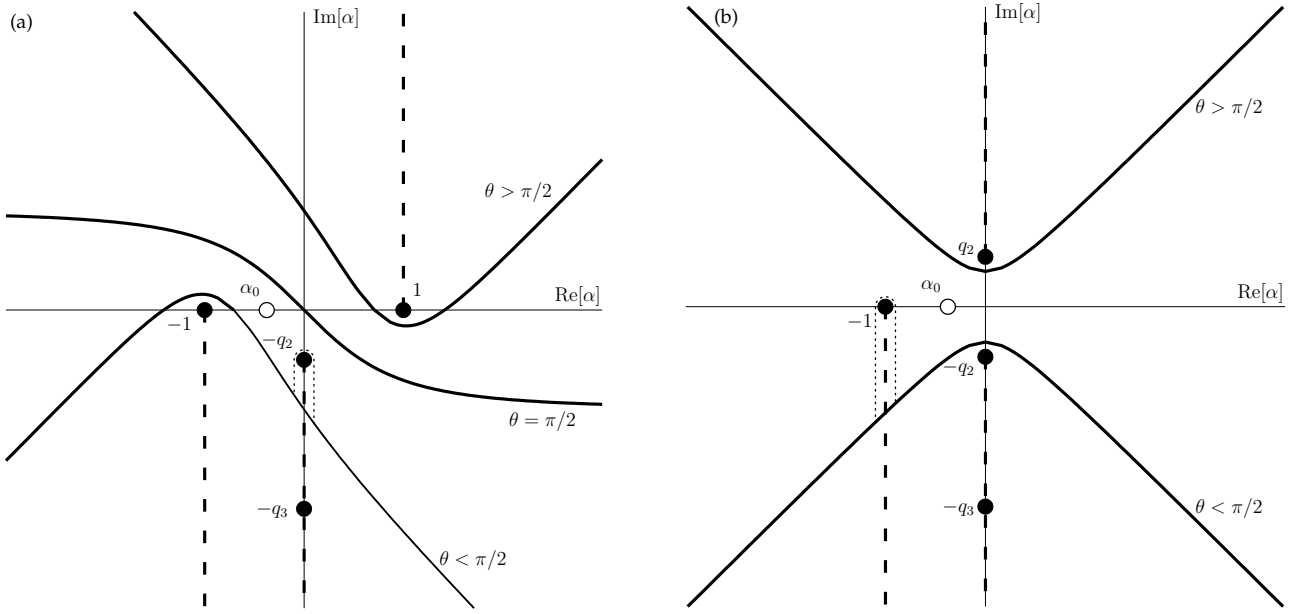


Figure S2: Steepest descents paths for (a)  $w_1$  (b)  $w_2$ . The dotted lines show the diversions around branch points needed for certain observation angles  $\theta$ . Note that the descent path for  $w_2$  in the case  $\theta = \pi/2$  is simply the real line.

we find that the descent paths can be parametrised via

$$\alpha = -\cos\theta(q_j + iv) \pm \sin\theta(v^2 - 2iq_jv)^{1/2}, \quad v \geq 0. \quad (\text{S9})$$

First consider the case  $j = 1$ , shown in figure S2a. If  $x < 0$  so that  $\cos\theta < 0$ , the steepest descents path lies predominantly in the upper half-plane, and there are no branch points to obstruct the deformation process (as  $\sin\theta \rightarrow 0$  the path wraps tightly around the cut emanating from  $\alpha = q_1 = 1$ ). The pole at  $\alpha = \alpha_0$  may lie to the right of the saddle point if  $\cos\theta < 0$ , in which case its residue must be collected, but this is addressed in the main body of the article. If  $x > 0$ , then a diversion is required if the descent path crosses the imaginary axis at or below  $-q_2$ , in order to retain the correct orientation with respect to the branch point. Writing  $\alpha = iu$  with  $u > 0$  in (S9) shows that this occurs if  $\cot\theta > |q_2|$ . The largest contribution comes from the branch point itself, and here the real part of the exponent is

$$r|q_2|\cos\theta \geq \frac{r|q_2|^2}{\sqrt{1+|q_2|^2}}. \quad (\text{S10})$$

Consequently, this contribution is exponentially small unless  $q_2 \approx 0$ , which occurs at high frequencies, such that the Mindlin model itself breaks down (see section 2). Therefore we may disregard the contribution from this diversion; the most significant contributions to  $w_1$  are due to the pole and the saddle.

The case  $j = 2$  in (S9), shown in figure S2b, is similar though slightly more complicated. Since  $q_2$  is positive imaginary, (99) shows that the integrand is exponentially small at the saddle point. For  $x < 0$ , the steepest descents path lies in the upper half-plane. Since the only singularity in the upper half-plane is the branch point at  $\alpha = q_2$ , there are no obstructions to deforming the integration contour onto the steepest descents path, and we may conclude that  $w_2 = O(e^{-|q_2|r})$ . For  $x > 0$ , the steepest descents path lies in the lower half-plane, and the residue from  $\alpha = \alpha_0$  is collected. The branch point at  $\alpha = -q_3$  does not interfere with the deformation of the path, but there is also a branch point at  $\alpha = -1$ , and the steepest descents path must be diverted around this. Now

$$\gamma_2(-1)|\sin\theta| - i\cos\theta = \sqrt{1 - q_2^2}|\sin\theta| - i\cos\theta, \quad (\text{S11})$$

meaning this contribution is exponentially small unless  $\sin\theta \approx 0$ . For  $\theta$  close to zero or  $2\pi$ , the branch point contribution is typically  $O(r^{-3/2})$ , because it can be related to an integral of the form

$\int_0^\infty \sqrt{s} e^{-rs} ds$ . This changes if the pole at  $\alpha = \alpha_0$  lies close to the branch point, in which case the contribution is  $O(r^{-1/2})$ , meaning the diversion does contribute to the field at leading order. This pole is only present for  $y < 0$  (see section 9). Thus  $w_2$  can contribute to the diffracted field at leading order if  $\Theta \approx 0$  and  $\theta \approx 2\pi$ . This is related to the breakdown of the uniform approximation (104) at the boundary in cases where  $\Theta \approx 0$ , noted in section 9.

## References

- [1] Wunsch AD. 2004 *Complex Variables with Applications*. Addison–Wesley third edition.